

THESIS FOR THE DEGREE OF LICENTIATE OF ENGINEERING

---

# Polarization in the ELAIS-N1 LOFAR deep field

SARA PIRAS



Department of Space, Earth, Environment  
Chalmers University of Technology  
Gothenburg, Sweden, 2023

# Polarization in the ELAIS-N1 LOFAR deep field

SARA PIRAS

Copyright © 2023 SARA PIRAS  
All rights reserved.

Technical Report No. 1111-111X  
ISSN 3.1415-9265  
This thesis has been prepared using L<sup>A</sup>T<sub>E</sub>X.

Department of Space, Earth, Environment  
Chalmers University of Technology  
SE-412 96 Gothenburg, Sweden  
Phone: +46 (0)31 772 1000  
[www.chalmers.se](http://www.chalmers.se)

Printed by Chalmers Reproservice  
Gothenburg, Sweden, February 2023

# Abstract

The physical characteristics of cosmic magnetic fields are encoded in the polarization properties of the extragalactic radio sources. Linearly polarized radiation undergoes Faraday rotation as it crosses a magneto-ionic medium; the rotation of the polarization angle of the signal is equal to its wavelength squared times the Rotation Measure (RM), that is proportional to the line-of-sight integral of the product of the magnetic field component along the line of sight and the density of thermal electrons. Mapping the values of the RM across the sky provides a mean to constrain cosmic magnetic fields. For this purpose, statistical studies of the properties of polarized radio sources spread over cosmological distances are essential.

The advantage of low radio-frequency observations over higher-frequency ones is the better precision on the inferred RM values. On the other hand, at low radio-frequency observations are more affected by depolarization, which affect the detection rate. Indeed, the population of faint polarized extragalactic sources at low radio frequencies is still mostly unknown.

In this context, the LOw Frequency ARray (LOFAR) plays an important role because of sensitivity, angular resolution and precision on the inferred RM values that can be achieved through low-frequency broad-band polarimetry, allowing us to study the polarized radio emission at frequencies around 150 MHz.

In our work, we developed a new method to combine polarimetric observations with slightly different frequency configurations, and we applied this method to the European Large Area ISO Survey-North 1 (ELAIS-N1) deep field, one of the deepest of the LOFAR Two-Meter Sky Survey (LoTSS) Deep Fields so far, at 114.9–177.4 MHz. We imaged an area of 25 deg<sup>2</sup> at 6-arcsec resolution in which, through stacking of 19 8-hour-long epochs, detected 1.28 sources per square degrees, the highest number density of polarized sources ever found at low radio frequencies. We compared our results with other RM catalogs and we quantified the depolarization properties of sources detected also at 1.4 GHz. We also modeled the source counts in polarization from the source counts in total flux density.

This work dealt with technical and theoretical challenges inherent to the observation and interpretation of polarimetric data and represents a step in solving complex issues that modern radio astronomy is facing due the large amounts of data generated by new-generation radio-interferometers.

**Keywords:** polarization – galaxies: individual (ELAIS-N1) – radio  
continuum: galaxies – techniques: polarimetric

## List of publications

This thesis is based on the following publication:

[A] **Piras S.**, Horellou C., et al., “LOFAR Deep Fields: Probing the sub-mJy regime of polarized extragalactic sources in ELAIS-N1”. To be submitted to *Astronomy & Astrophysics (A&A)*.

Other publications by the author, not included in this thesis, are:

[B] Herrera Ruiz N., O’Sullivan S. P., Vacca V., Jelić V., Nikiel-Wroczyński B., Bourke S., Sabater J., Dettmar R.-J., Heald G., Horellou C., **Piras S.**, Sobey C., Shimwell T. B., Tasse C., Hardcastle M. J., Kondapally R., Chyży K. T., Iacobelli M., Best P. N., Brüggén M., Carretti E., and Prandoni I., “LOFAR Deep Fields: probing a broader population of polarized radio galaxies in ELAIS-N1”. *Astronomy & Astrophysics*, Volume 648, id.A12.

[C] Šnidarić I., Jelić V., Mevius M., Brentjens M., Erceg A., Shimwell T. W., **Piras S.**, Horellou C., Sabater J., Best P. N., Bracco A., Ceraj L., Haverkorn M., O’Sullivan S. P., Turić L, and Vacca V., “LOFAR Deep Fields: Probing faint Galactic polarized emission in ELAIS-N1”. Submitted at *Astronomy & Astrophysics*.



---

# Contents

---

<b>Abstract</b>	<b>i</b>
<b>List of Papers</b>	<b>iii</b>
<b>I Overview</b>	<b>1</b>
<b>1 Introduction</b>	<b>3</b>
1.1 Magnetic fields in the large scale structure . . . . .	3
Synchrotron radiation . . . . .	4
Extragalactic radio sources . . . . .	5
<b>2 Polarization and Faraday rotation</b>	<b>9</b>
2.1 Polarization and Stokes parameters . . . . .	10
2.2 Faraday rotation . . . . .	12
The effect . . . . .	12
The Faraday Rotation Measure Synthesis Technique . . . . .	14
2.3 Depolarization . . . . .	17
2.4 Rotation Measure Grid . . . . .	21
<b>3 Polarized source counts</b>	<b>25</b>
3.1 Definition . . . . .	27

3.2	Measurements in total flux density and polarized flux density . . . . .	30
3.3	Modeling source counts in polarization . . . . .	33
<b>4</b>	<b>Polarization with LOFAR</b>	<b>37</b>
4.1	LOFAR . . . . .	37
4.2	Constrain cosmic magnetic fields with LOFAR . . . . .	40
<b>5</b>	<b>Polarization in the ELAIS-N1 LOFAR Deep Field</b>	<b>43</b>
5.1	The European Large-Area ISO Survey-North 1 (ELAIS-N1) . . . . .	43
5.2	The ELAIS-N1 LOFAR Deep Field . . . . .	44
5.3	Observations . . . . .	45
5.4	Stacking polarization data . . . . .	46
	Noise . . . . .	47
	The stacking method . . . . .	50
	Manage big data . . . . .	53
<b>6</b>	<b>Paper summary</b>	<b>57</b>
<b>7</b>	<b>Summary and future work</b>	<b>59</b>
	<b>Bibliography</b>	<b>61</b>
<b>II</b>	<b>Paper</b>	<b>67</b>
<b>A</b>	<b>Pol. in ELAISN-1</b>	<b>A1</b>

# Part I

# Overview



# CHAPTER 1

---

## Introduction

---

### 1.1 Magnetic fields in the large scale structure

Magnetic fields permeate the Universe across all scales and over all of cosmic time, but our knowledge and understanding of many of the properties of magnetic fields and their origin are still limited.

The magnetic fields associated with the large scale structure of the Universe are referred as intergalactic magnetic fields (IGMF). IGMF are very weak: the range of values is from tenths of  $\mu\text{G}$  (Kronberg et al. 2007; Xu et al. 2006) to a lower limit of  $3 \times 10^{-16}$  G (Neronov & Vovk 2010), and they are difficult to observe because they need to be "illuminated". A way to probe the IGMF is through radio lobes and jets of Active Galactic Nuclei (AGN), a class of extragalactic radio sources that we will introduce in Sec. 1.1. AGN allow to investigate phenomena associated with magnetized plasmas and they are known to emit linear polarized radiation that arises from synchrotron processes, that we introduce in Sec. 1.1. The polarized emission of background AGN, whose properties we will introduce in Chapter 2, interacts with the cosmic magnetic field along the line of sight, making it possible to probe them. AGN are used as extragalactic background sources to investigate the magneto-ionic medium

along the line of sight between the source of emission and us. A dense all-sky grid of extragalactic background polarized sources, a so-called *RM grid* that we will introduce in Sec. 2.4, will help us in mapping and studying the magnetic fields in our Universe. The largest all-sky RM grid actually available was obtained by Taylor et al. (2009) at 1.4 GHz, who found an average number density of about one source per square degree. The interaction between polarized emission and magneto-ionized plasmas is greater at low frequencies, however depolarization phenomena are stronger, making the detection of this radiation much more challenging. The LOw Frequency ARray (LOFAR), the planned Square Kilometre Array (SKA) and its precursor telescopes, the Australia SKA Pathfinder (ASKAP) and the Karoo Array Telescopes (MeerKAT) in South Africa, are large next-generation radio telescopes developed to perform broad-bandwidth polarimetric observations at low radio frequencies over large areas of the sky at high sensitivity and high resolution, and will permit to build a denser RM grid and explore cosmic magnetism.

## Synchrotron radiation

Radio synchrotron emission from discrete radio sources is a non-thermal process. The theory associated with these emission mechanisms is well explained and developed in the literature; a detailed description can be found *Radiative processes in astrophysics* by Rybicki & Lightman (1979) and *Galactic and Intergalactic Magnetic Fields* by Klein & Fletcher (2015), from which the information in this section is taken.

Relativistic charged particles moving in a magnetic field undergo a helical motion, a combination of a circular motion in the plane perpendicular to the magnetic field lines and a linearly uniform motion in the direction of the magnetic field; radiative losses are caused by the acceleration of these particles. The synchrotron radiation produced by a single charge, due to the relativistic beaming effect, appears to be half-concentrated in a cone with a half-width of about  $\gamma^{-1}$ , where  $\gamma$  is the Lorentz factor defined as  $\gamma = 1/\sqrt{1-v^2/c^2}$ , which has as its axis the instantaneous direction of the velocity of the emitting particle, while the other half is essentially diluted over the entire solid angle.

The study of this radiation is possible by formulating some hypotheses on the physical conditions of the emitting plasma, in particular the energy density of the particles and of the magnetic field present, since the observation of the radiation alone provides information on the global interaction but not on

the individual components that produce the emission. From observations of cosmic rays on Earth it is known that the energy spectrum in the Milky Way can be described by a power law:

$$N(E)dE \propto E^{-g}dE \quad (1.1)$$

with  $g \approx 2.4$ . The specific intensity associated with this energy distribution is:

$$I_\nu \propto B_\perp^{1-\alpha} \cdot \nu^\alpha \quad (1.2)$$

where  $B_\perp$  is the magnetic field component perpendicular to the line of sight and  $\alpha$  is the spectral index, which is related to the exponent,  $g$ , of the power-law spectrum of the cosmic-ray electrons:

$$\alpha = \frac{1-g}{2} \quad (1.3)$$

In the case of the Milky Way, the spectral index is  $\alpha \approx -0.7$ .

## Extragalactic radio sources

The extragalactic objects which are sources of synchrotron radiation and on which we will focus are the radio galaxies and quasars. Both sources are classified as AGN and represent some of the most powerful sources of energy in the Universe, whose emission may cover the entire electromagnetic spectrum, from the radio band up to the  $\gamma$ -rays. The synchrotron emission originates in the AGN, which host a supermassive black hole (SMBH). The energy that powers the radio sources is released from the AGN in the form of relativistic jets of plasma. The ultimate source of this energy is the release of gravitational potential energy due to the infall of matter onto a SMBH, centered in the host galaxy's core (Blandford & Rees 1974).

We will introduce the properties of radio galaxies, quasar and blazar following *Galactic and Intergalactic Magnetic Fields* by Klein & Fletcher (2015).

### Radio galaxies

Radio galaxies are almost exclusively associated with elliptical galaxies. The radio emission arises from by a pair of initially relativistic plasma jets that propagate in opposite directions outside the host galaxy, through the inter-

galactic medium. Interaction with the external gas slows down the jets and may deflect them, giving rise to a variety of radio structures. In many cases, the plasma slows down into ellipsoidal lobes that surround the radio jets.

Radio galaxies are very strong radio emitters, with radio luminosities  $L_{\text{radio}}$  greater than  $3 \times 10^{41} \text{ erg s}^{-1}$ ; the lobes can have dimensions of hundreds of kpc and accumulate energies in relativistic particles and magnetic fields form. The synchrotron emission we observe arises from relativistic particles with energies of  $\sim \text{GeV}$  gyrating around magnetic fields of strengths of the order of  $10 \mu\text{G}$ .

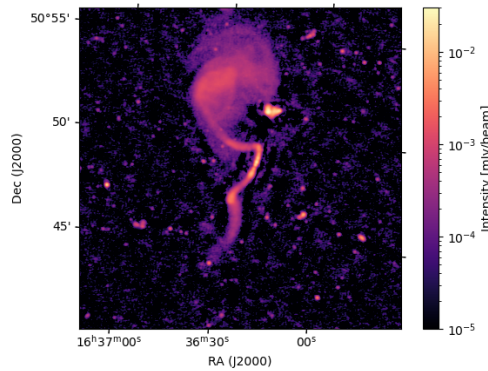


**Figure 1.1:** Radio galaxy in the LOFAR ELAIS-N1 deep field at 150 MHz. From Sabater et al. (2021).

Radio galaxies can assume a large variety of shapes and sizes, from the most compact (few pc) to the most complex structure covering hundreds of kpc. Traditionally, they are classified as “Fanaroff-Riley” (FR) type I and type II (Fanaroff & Riley 1974):

- FR II radio galaxies are most powerful radio sources with bright outer parts, and are called edge-brightened, due to the presence of compact hot-spots (sometimes even  $< 1 \text{ kpc}$ ) which are generally aligned with the central optical object. The lobes are well separated, longer than wide. Sometimes they show weak and well collimated jets, and in about 10% of the sources only one jet is seen. They are usually associated with quasars or distant galaxies. FR II radio galaxies have monochromatic radio luminosities of  $L_{1.4\text{GHz}} \geq 10^{32} \text{ erg s}^{-1} \text{ Hz}^{-1}$ .
- FR I radio galaxies are weaker radio sources, the hot-spots are weak

or absent. The lobes are not always so well aligned with the central object; they are generally quite large compared to the total dimensions of the radio source and often almost in contact. Sometimes they also show more or less pronounced distortions in the structure. The radio core also tends to be brighter in percentage terms. At low resolution these characteristics make them appear with a higher brightness in the central part, which then slowly decreases away from the nucleus. This is why they are called edge-darkened. They are generally associated with nearby galaxies and/or found in clusters of galaxies. FRI radio galaxies have monochromatic radio luminosities of  $L_{1.4 \text{ GHz}} \leq 10^{32} \text{ erg s}^{-1} \text{ Hz}^{-1}$ .

The morphology of the lobes depends on their interaction with the medium into which they are expanding. At low radio frequencies, the number of de-

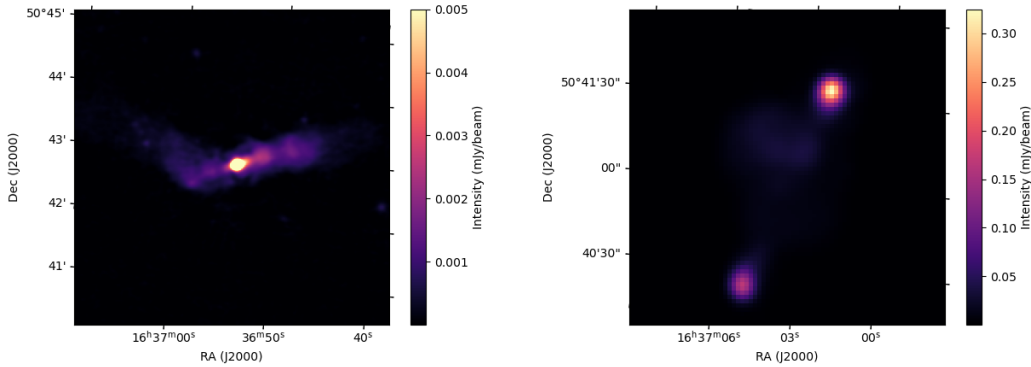


**Figure 1.2:** Example of sources with morphologies similar to a FRI (left panel) and a FRII (right panel) radio galaxies, detected in the LOFAR ELAIS-N1 deep field at 150 MHz. From Sabater et al. (2021).

tected polarized FRII radio sources is generally greater than that of FRI (Van Eck et al. 2018), however it has been demonstrated by Herrera Ruiz et al. (2021) that the number of the latter increases with increasingly sensitive observations. We show in Fig. 1.2 two examples of two sources with morphologies similar to FRI and FRII radio galaxies in the ELAIS-N1 deep field (Sabater et al. 2021). In the left panel we can see that the nucleus is brighter than the jets, instead in the right panel the nucleus is not visible but we can see easily the hotspots and some diffuse emission in the lobes. In our work we detect polarized emission from the nucleus of the first radio galaxy and from both the hotspots of the second one.

## Radio quasars

Historically, quasars were identified as star-like extragalactic objects (quasi-stellar object, QSO) with broad lines in their optical spectra. Some quasars are visible from radio wavelengths through X-ray energies, are the most luminous class of AGNs and the most luminous objects in the Universe, reaching luminosities from  $10^{45}$  to  $10^{49}$  erg  $s^{-1}$ . The most accredited hypothesis foresees that they are connected to a period of violent merging of massive galaxies in the course of structure formation of the Universe, peaking at redshift  $z \approx 2$  and truncating in formation below  $z \approx 0.4$ . Not all quasars are also strong radio synchrotron sources, and with respect to this characteristic there are 'radio-quiet', that are the majority of QSOs, and 'radio-loud' quasars. Radio-loud quasars show one-sided jets, which sometimes produce large-scale lobes too. In the left panel of Fig. 1.3 we show an example of a quasar in the ELAIS-N1 deep field (Sabater et al. 2021). We found this quasar to be polarized.

## Blazars

Blazars exhibit strong variability and are most likely AGN in which we are looking almost directly into the jet coming towards us, which results in relativistic boosting, the so-called 'Doppler boosting'. In the right panel of Fig. 1.3 we show an example of a blazar detected in the ELAIS-N1 deep field that we found to be polarized.

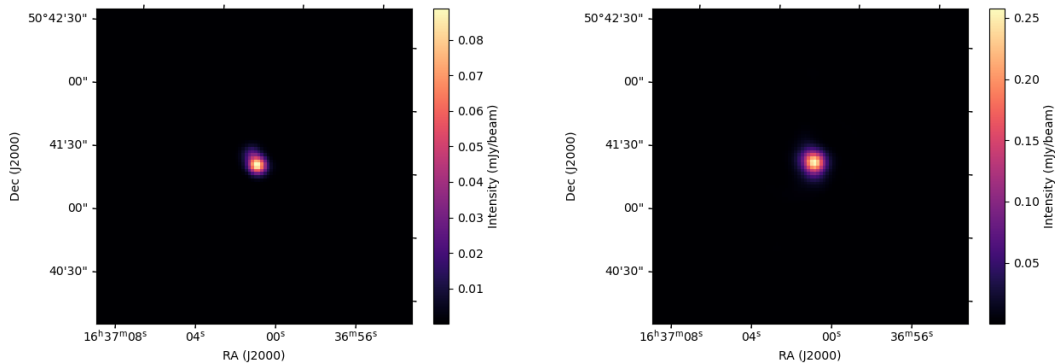


**Figure 1.3:** Example of quasar (left panel) and a blazar (right panel) in the LOFAR ELAIS-N1 deep field at 150 MHz. We found these two sources to be polarized. From Sabater et al. (2021).

## CHAPTER 2

---

### Polarization and Faraday rotation

---

Synchrotron radiation is linearly polarized: since the direction of motion corresponds to the direction of emission, the radiation must be linearly polarized if we observe exactly along the plane of the orbit of the charged particle when the electron moves towards us. Elliptically polarized radiation (i.e. with a linear and a circular component), but of lower intensity, occurs when the line of sight is slightly out of the plane but always within the  $\gamma^{-1}$  half-amplitude cone of radiation. The direction of the electric vector in the case of linear polarization, or of the major axis of the ellipse in the case of elliptical polarization, is in the plane of the orbit of the charged particle and is therefore perpendicular to the direction of the magnetic field present. We receive radiation from a plasma of relativistic electrons only from those whose velocities form an angle  $\leq \gamma^{-1}$  with the line of sight and if the magnetic field is ordered the radiation is still polarized. Since the velocities of the electrons are introduced into the field are generally disordered, and therefore are all different from each other, the planes of the orbits "useful" for receiving radiation will all be slightly different. The polarization ellipses will be equally right-hand and left-hand polarized, so the contributions of circular polarization will tend to cancel out on average. Therefore it will remain a state of linear polarization,

with the electric vector still perpendicular to the magnetic field.

In most real cases, the magnetic field is not uniform and the polarization percentage of the radiation can be greatly reduced: regions with differently oriented magnetic fields give rise to differently oriented polarization vectors; these, averaging along the line of sight and in the beam of the observation instrument, tend to cancel out. The polarization percentage therefore is related to the degree of order of the magnetic field in the radio source or in the medium in which the emission is propagating.

The total and the polarized radio emission are described by the Stokes parameters, that we will introduce in the following Sec. 2.1.

The interaction between the polarized emission and a magneto-ionic medium causes the effect called Faraday rotation, which we will deepen in Sec. 2.2.

## 2.1 Polarization and Stokes parameters

The radio emission can be empirically quantified using the Stokes parameters; for a more detailed discussion see *Tools of Radio Astronomy* by Wilson et al. (2013), *Essential Radio Astronomy* by Condon & Ransom (2016) and Heiles (2002).

We can write the projected electric field vector in the  $(x, y)$  plane of a monochromatic wave that is propagating in the the  $z$ -direction as:

$$\vec{E} = [\vec{E}_x \exp(i\phi_x)\hat{x} + \vec{E}_y \exp(i\phi_y)\hat{y}] \exp[i(\vec{k} \cdot \vec{z} - \omega t)] \quad (2.1)$$

where  $t$  represents the time,  $E_x$  and  $E_y$  are the projections of  $\vec{E}$  in the  $(x, y)$  plane,  $\omega = 2\pi\nu$  is the angular frequency,  $k = 2\pi/\lambda$  is the wave number, and  $\phi_x$  and  $\phi_y$  are constant phases that define the phase difference  $\delta = \phi_x - \phi_y$ .

The electric field  $\vec{E}$  at any time-independent combination of phases and amplitudes draws an ellipse in the  $(x, y)$  plane and the wave is called *elliptically polarized*, as shown in Fig. 2.1.

Measurements are sensitive to the power of a radiation, i.e. the time average of the square of the electric field or the time average of the product of the electric field with its complex conjugate. In particular, this is expressed through the *Stokes parameters*.

The Stokes parameters are linear combinations of power measures of independent orthogonal polarizations and denoted as  $I$ ,  $Q$ ,  $U$  and  $V$ ; they can

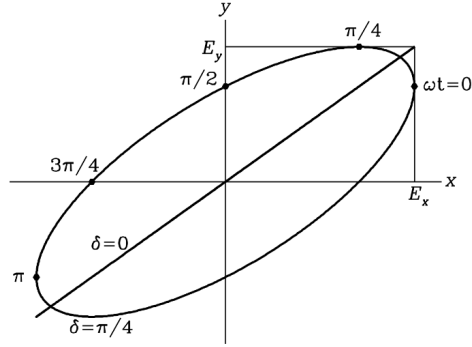


**Figure 2.1:** Example of ellipse drawn by the electric field vector  $\vec{E}$  in Eq. 2.1 in the  $(x, y)$  plane and propagating in the  $z$ -direction. If  $\delta=0$ ,  $\vec{E}$  does not rotate and the wave is called *linearly polarized*. If  $E_x = E_y$  and  $\delta = \frac{\pi}{2}$ ,  $\vec{E}$  draws a circle and the wave is called *circularly polarized*. Image from the book *Essential Radio astronomy* by Condon & Ransom (2016).

describe a completely polarized light, but also unpolarized light and partially polarized light. They are defined as:

- $I = \langle E_x E_x^* + E_y E_y^* \rangle$
- $Q = \langle E_x E_x^* - E_y E_y^* \rangle$
- $U = \langle E_x^* E_y + E_x E_y^* \rangle$
- $iV = \langle E_x^* E_y - E_x E_y^* \rangle$

where the brackets  $\langle \rangle$  denote a time average, the apex \* the complex conjugate and  $i$  the imaginary unit.

The Stokes parameter  $I$  quantifies the total intensity of the field;  $Q$  describes the preponderance of linearly horizontally polarized radiation over linearly vertically polarized radiation;  $U$  describes the preponderance of linear  $+45^\circ$  polarized radiation over linear  $-45^\circ$  polarized radiation;  $V$  quantifies the preponderance of right circularly polarized radiation ( $\vec{E}$  rotates clockwise) over left circularly polarized radiation ( $\vec{E}$  rotates anti-clockwise).

The fractional linear polarization is defined as the ratio of the intensity of the linearly polarized emission to the total intensity:

$$p = \frac{\sqrt{Q^2 + U^2}}{I}; \quad 0 \leq p \leq 1 \quad (2.2)$$

As synchrotron radiation is linearly polarized, we can assume  $V = 0$ . The linearly polarized intensity can be written as a complex number:

$$P = Q + iU = pIe^{2i\chi} \quad (2.3)$$

where  $\chi$  is called *polarization angle* and is defined as a function of the Stokes parameters:

$$\chi = \frac{1}{2} \tan^{-1} \left( \frac{U}{Q} \right) \quad (2.4)$$

The polarized signal is a fraction of the total signal. Considering an isotropic distribution of speeds and a uniform magnetic field, it is calculated that the intrinsic linear polarization fraction  $p = (g+1)/(g+7/3)$ , where  $g$  is the index of the power-law of the energy distribution of relativistic electrons (Eq. 1.1); in the case of the Milky Way we can expect a maximum degree of linear polarization of a synchrotron source of  $p = 72\%$ . Most sources show considerably lower polarization at radio frequencies. Indeed if the magnetic field is not spatially uniform, as happens in real astronomical cases, the polarization percentage can be greatly reduced, since the contributions originating in regions where the magnetic field has different orientations have, in turn, polarizations differently oriented; those, averaging along the line of sight, or within the solid angle defined by the resolving power of the observation instrument, tend to cancel out.

## 2.2 Faraday rotation

### The effect

Linearly polarized electromagnetic radiation, propagating in a magneto-ionic medium, undergoes a rotation of its polarization plane. This effect is called Faraday rotation. A detailed derivation of Faraday rotation can be found in plasma physics textbooks, as Choudhuri (1998), Gurnett & Bhattacharjee (2005) and in appendix D of *Essential Radio Astronomy* by Condon & Ransom (2016).

A linearly polarized wave is a superposition of a right-hand and left-hand circularly polarized waves. When these two components propagate through a magnetized plasma, the relative phase between them changes as the waves propagate, causing linearly polarized wave to change its polarization angle

during the propagation.

The polarization angle of a linearly polarized emitting is strongly dependent on the wavelength at which the emission is measured:

$$\chi = \chi_0 + \text{RM} \cdot \lambda^2 \quad (2.5)$$

where  $\chi$  and  $\chi_0$  are respectively the observed and the intrinsic polarization angles, and RM is the rotation measure. Traditionally, the determination of RMs has been done by observing the polarization angle at different wavelengths, and then determining the slope of  $\chi$  in the  $\lambda^2$ -space. In the ideal case of a non synchrotron emitting plasma screen being the only source for the Faraday rotation effect, the RM is equal to the Faraday depth:

$$\phi(l) = \frac{e^3}{8\pi^2 m_e^2 c^3 \epsilon_0} \int_{\text{source}}^{\text{observer}} B_{\parallel} n_e dl \quad (2.6)$$

where  $e$  and  $m_e$  are, respectively, the charge and the mass of the electron,  $c$  is the speed of light,  $\epsilon_0$  is the permittivity of free space,  $B_{\parallel}$  is the line-of-sight component of the magnetic field in the foreground medium,  $n_e$  is the thermal plasma electron density and  $l$  is path length from the source to the observer. A positive value of Faraday depth corresponds to a magnetic field pointing towards the observer.

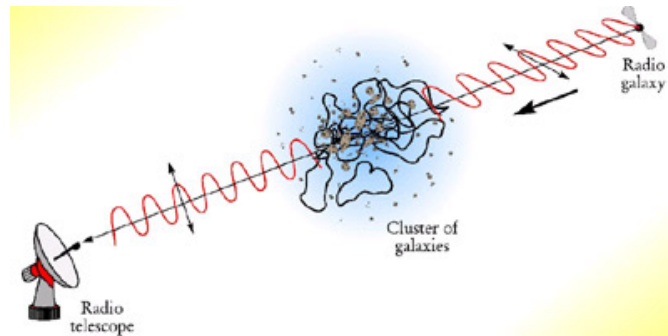


**Figure 2.2:** Cartoon of the Faraday rotation effect on the polarized emission of a background radio galaxy caused by the magneto-ionic medium of a galaxy cluster. Credits: <https://www.skatelescope.org/>

In convenient units, the Faraday depth can be expressed as:

$$\left(\frac{\phi(l)}{\text{rad m}^{-2}}\right) = 0.812 \int_{\text{source}}^{\text{observer}} \left(\frac{B_{\parallel}}{\mu\text{G}}\right) \left(\frac{n_e}{\text{cm}^{-3}}\right) \left(\frac{dl}{\text{pc}}\right) \quad (2.7)$$

The measurement of the Faraday depth of a source that emits linearly polarized waves is carried out by observing its polarization angle at different wavelengths. In Fig. 2.3 we show the polarization angle  $\chi$  in function of the wavelength squared ( $\text{m}^2$ ) for a polarized source found in our work. The slope of  $\chi$  versus  $\lambda^2$  is the RM. The effect of Faraday rotation is clearly visible in the variation of  $\chi$ ; the loss of definition of the slope is a sign of Faraday depolarization, which we will discuss in the Sec. 2.3.

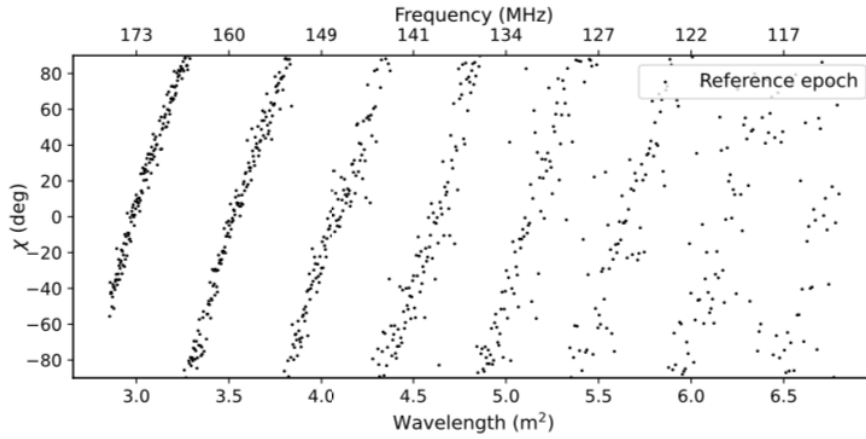


**Figure 2.3:** Polarization angle  $\chi$  versus wavelength squared  $\lambda^2$  for a source found polarized in our data. The rotation of the polarization angle is caused from the Faraday effect, and its slope is the RM. The legend indicates the epoch to which the data belong (More details in Sec. 4).

If the polarized wave is emitted by a source and then passes through a non synchrotron emitting magneto-ionic cloud along the line of sight, the rotation measure RM is equal to the Faraday depth  $\phi$ .

## The Faraday Rotation Measure Synthesis Technique

A fundamental point in the mapping and characterization of polarized sources is the determination of their rotation measures. Traditionally, RM has been determined by plotting the observed polarization angle as a function of the

square of the observing wavelength (at least two), and performing a least-squares fit to the data. This approach carries potential problems (see Heald 2009; Burn 1966; Brentjens & de Bruyn 2005):

1. having polarization angles available at only a few observing wavelengths, the resulting RM values can be ambiguous because of wrapping(s) of polarization angles in these bands. This is the so-called  $n\pi$ -ambiguity problem;
2. polarized emission from radio sources with different Faraday depth  $\phi(l)$  values, and then different RM values, can be present in a single line of sight. The signal from these different components mixes, making a linear fit inappropriate;
3. we would not have polarization angles available for a linear fit for faint source with high RM; these sources would be undetectable in the single channels due to the low signal-to-noise ratio, and they would not be detectable even by averaging all the channels due to bandwidth depolarization.

The rotation measure synthesis technique (Burn 1966; Brentjens & de Bruyn 2005) permits to overcome this problem. In this technique, the complex Faraday dispersion function  $F(\phi)$  is introduced and defined as:

$$P(\lambda^2) = \int_{-\infty}^{\infty} F(\phi) e^{2i\phi\lambda^2} d\phi . \quad (2.8)$$

$F(\phi)$  describes the intrinsic polarized flux, as a function of the Faraday depth, so here we highlight that the observed polarization vector originates from emission at all possible values of  $\phi$ . Eq. 2.8 has the form of a Fourier transform, that could, in principal, be inverted to find the intrinsic polarization in terms of observable quantities:

$$F(\phi) = \int_{-\infty}^{\infty} P(\lambda^2) e^{-2i\phi\lambda^2} d\lambda^2 \quad (2.9)$$

if one makes assumption on the value on  $P(\lambda^2)$  for  $\lambda^2 < 0$ , indeed it has physical meaning only for wavelengths  $\lambda^2 \geq 0$ . In this context, Brentjens & de Bruyn (2005) introduce the weight function  $W(\lambda^2)$ , which is equal to 1 if

$P(\lambda^2)$  is measured and 0 otherwise. So the observed polarized emission can be expressed as:

$$\tilde{P}(\lambda^2) = W(\lambda^2)P(\lambda^2) = W(\lambda^2) \int_{-\infty}^{\infty} F(\phi)e^{2i\phi\lambda^2} d\phi \quad (2.10)$$

The reconstructed Faraday dispersion function is then:

$$\tilde{F}(\phi) = K \int_{-\infty}^{\infty} \tilde{P}(\lambda^2)e^{-2i\phi\lambda^2} d\lambda^2 = F(\phi) * R(\phi) \quad (2.11)$$

with  $K = \left( \int_{-\infty}^{\infty} W(\lambda^2)d\lambda^2 \right)^{-1}$ . Here  $*$  is the convolution operation and  $R(\phi)$  is the Rotation Measure Transfer Function (RMTF). The RMTF is expressed as:

$$R(\phi) = K \int_{-\infty}^{\infty} W(\lambda^2)e^{-2i\phi\lambda^2} d\lambda^2 \quad (2.12)$$

therefore it does contain only information about the measurement conditions.

If, for each of the  $N$  observed frequency channels,  $\phi d\lambda^2 \ll 1$ , the rotation measure synthesis technique can be implemented using the equations:

$$\tilde{F}(\phi) \approx K \sum_{i=1}^N \tilde{P}_i e^{-2i\phi(\lambda_i^2 - \lambda_0^2)} \quad (2.13)$$

$$R(\phi) \approx K \sum_{i=1}^N W_i e^{-2i\phi(\lambda_i^2 - \lambda_0^2)} \quad (2.14)$$

$$K = \left( \sum_{i=1}^N w_i \right)^{-1} \quad (2.15)$$

where  $\lambda_i^2$  is the  $\lambda^2$  that corresponds to the central frequency of the channel  $i$ ,  $\tilde{P}_i = \tilde{P}(\lambda_i^2) = w_i P(\lambda_i^2)$  and  $w_i = W(\lambda_i^2)$ . The constant shift  $\lambda_0^2$  is the weighted average of the observed  $\lambda^2$  and is introduced to attenuate the oscillations of the real part of the reconstructed approximation to the Faraday dispersion function and RMTF. Indeed, the real and imaginary parts of the RMTF have big oscillations in the main maximum, and it can make difficult to calculate the polarization angle  $\chi$ .

The RM synthesis technique uses a series of trial RM values and find the

one which maximizes the signal level resulting from the coaddition of the polarized flux from all channels. The flux as a function of  $\phi$ ,  $\tilde{F}(\phi)$ , peaks at the value of  $\phi$  corresponding to the RM of the source. At other values of  $\phi$ , the polarization vector will not constructively interfere throughout the band, and the total flux will be lower. The RM synthesis minimizes the  $n\pi$  ambiguity by taking advantage of the many individual narrow frequency channels: only the brightest polarized emission would be detected above the noise level in each narrow frequency channel, whereas the signal becomes concentrated in a narrow range in Faraday space,  $\tilde{F}(\phi)$ . The RM synthesis is also capable of detecting emissions at multiple Faraday depths along a particular line of sight, which helps to distinguish the contributions from different objects along the same line of sight.

The theoretical limits for what is possible to detect with RM synthesis involve the channel width  $\delta\lambda^2$ , the width of the distribution  $\Delta\lambda^2$  in  $\lambda^2$ -space, and the shortest wavelength squared  $\lambda_{\min}^2$ . For a top-hat weight function which is 1 between  $\lambda_{\min}^2$  and  $\lambda_{\max}^2$  and zero elsewhere, we can estimate the resolution in Faraday space  $\delta\phi$ , the maximum observable Faraday depth *maxscale* and the largest scale in  $\phi$  space to which one is sensitive:

$$\delta\phi \approx \frac{2\sqrt{3}}{\Delta\lambda^2} \quad (2.16)$$

$$\text{maxscale} \approx \frac{\pi}{\lambda_{\min}^2} \quad (2.17)$$

$$\|\phi_{\max}\| \approx \frac{\sqrt{3}}{\delta\lambda^2} \quad (2.18)$$

The maximum scale, *maxscale*, gives the upper limit to which structures in  $\phi$ -space which are smaller than the maximum scale can be resolved, but larger structures are not detected as a whole structure. The largest scale in  $\phi$ -space to which one is sensitive,  $\|\phi_{\max}\|$ , gives the maximum value in  $\phi$ -space which can be detected with a sensitivity greater than 50%.

## 2.3 Depolarization

Faraday rotation can cause a frequency-dependent reduction in the fractional polarization; this phenomenon is called Faraday depolarization. Depolariza-

tion of the radiation can be due to inhomogeneities of the magnetic field or the distribution of thermal electrons with which the wave interacts.

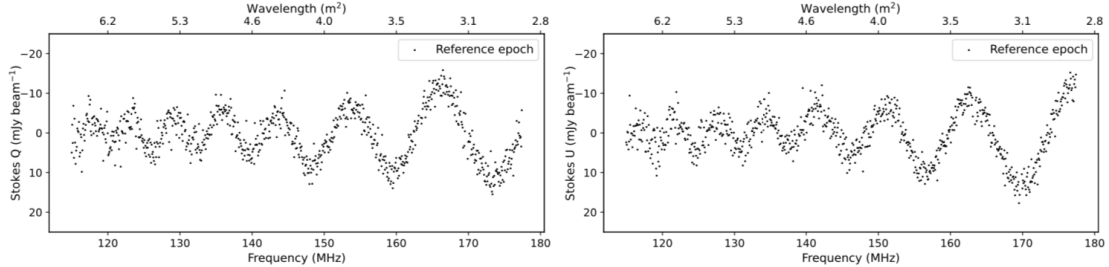


**Figure 2.4:** Example of a polarized source found in our work. Left panel: Stokes  $Q$  intensity as a function of frequency and wavelength squared  $\lambda^2$  (bottom and top axes). Right panel: Stokes  $U$  intensity as a function of frequency and wavelength squared  $\lambda^2$  (bottom and top axes). The effect of Faraday depolarization is visible in the decrease of the amplitude at lower frequencies (longer wavelengths). The legend indicates the epoch to which the data belong (more details in Sec. 4).

Faraday depolarization can take place inside the source, and/or be produced during propagation in the external medium. The observed fractional polarization,  $p$ , is different from the intrinsic fractional polarization,  $p_0$ .

A detailed discussion of depolarization processes can be found in Burn (1966) and Sokoloff et al. (1998).

The most common depolarization mechanisms are:

- *Internal Faraday dispersion:* Faraday rotation can occur inside radio sources or the magneto-ionic medium along the line of sight if they contain thermal plasma and turbulent and/or filamentary magnetic fields. In this case, in addition to the rotation of the polarization plane there is also a reduction the percentage of polarization. This can be understood considering that the radiation coming from the most distant regions will undergo a greater Faraday rotation than that emitted by the regions close to the observer. Consequently, the different radiation contributions will reach the observer with different polarization angles, even if they originally had the same intrinsic angle. The sum of all these contributions will therefore be less than the sum of the amplitudes alone (as would be the case if the emission from each region were subject to the same Faraday rotation), and the global polarization will be reduced. The

observed fractional polarization depends on the RM dispersion along the line of sight,  $\sigma_{\text{RM}}$  and the fractional polarization can be described by:

$$p(\lambda) = p_0 \frac{1 - e^{-2\sigma_{\text{RM}}\lambda^4}}{2\sigma_{\text{RM}}\lambda^4} \quad (2.19)$$

- *External Faraday dispersion:* it occurs when the radiation emitted by the source passes through an inhomogeneous external medium (thermal electrons and turbulent and/or filamentary magnetic fields but not relativistic electrons). The radiation coming from regions of the source crosses the external medium, the *Faraday screen*, undergoing different Faraday rotations, in a random way, from region to region. The background sources is depolarized because the emission crossing different paths is diluted in the observing beam, and the observed fractional polarization is:

$$p(\lambda) = p_0 e^{-2\sigma_{\text{RM}}^2\lambda^4} \quad (2.20)$$

- *Differential Faraday rotation:* in this case the emitting and Faraday rotating regions are co-spatial and host a regular magnetic field. The polarization plane of the emission at the far side of the region undergoes a different amount of Faraday rotation compared to the polarized emission coming from the near side, causing depolarization when summed along the line of sight. The observed fractional polarization can be described as:

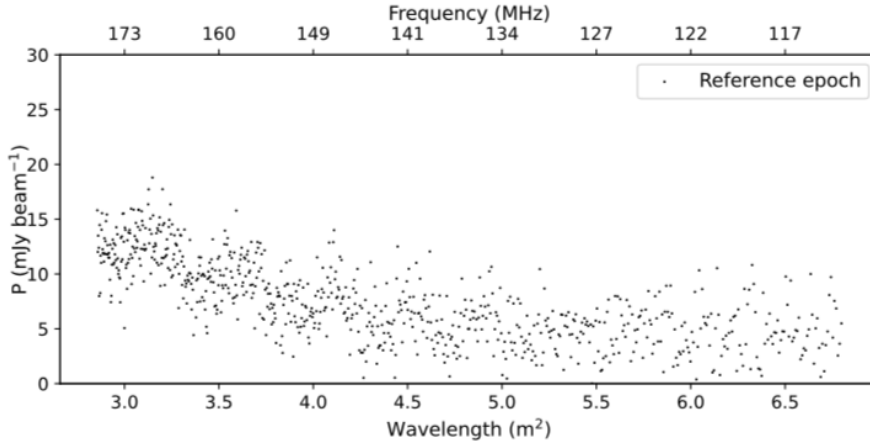
$$p(\lambda) = p_0 \frac{|\sin(2\langle\text{RM}\rangle\lambda^2)|}{2\langle\text{RM}\rangle\lambda^2} \quad (2.21)$$

- *Bandwidth depolarization:* if a frequency channel is wide enough, or if many channels are averaged, the polarization angle may vary sufficiently within a channel or within the considered frequency band to cause depolarization.
- *Beam depolarization:* different polarization components are in the same line of sight and within the telescope main beam, so they cannot be resolved.

Fig. 2.4 shows the measured Stokes  $Q, U$  parameters as a function of frequency and wavelength squared  $\lambda^2$  (bottom and top axes) for the polarized

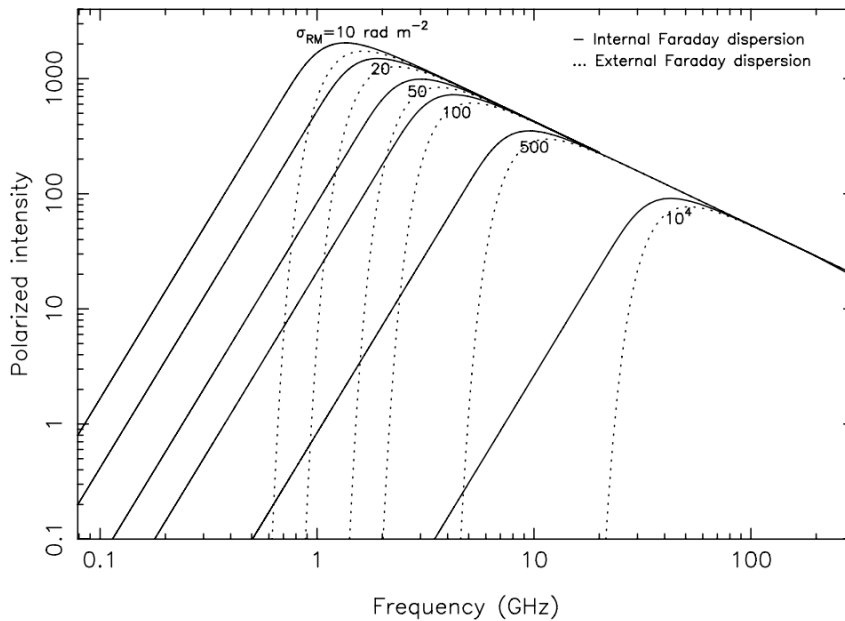
source of Fig. 2.3. The effect of Faraday depolarization is visible in the decrease of the amplitude at lower frequencies (longer wavelengths).

Fig. 2.5 shows the polarized intensity  $P$  as function of frequency and wavelength squared  $\lambda^2$  and frequency (bottom and top axes) for the same source of Fig. 2.3. This source is affected by depolarization that highlighted by the decrease of the polarized intensity with  $\lambda^2$ .



**Figure 2.5:** Polarized intensity  $P$  as a function of wavelength squared  $\lambda^2$  and frequency (bottom and top axes) for one of our polarized sources in ELAIS-N1. The effect of Faraday depolarization is visible in the decrease of the polarized intensity with  $\lambda^2$ . The legend indicates the epoch to which the data belong (details in Sec. 4).

We show in Fig. 2.6 the polarized intensity for a total-intensity synchrotron emission of spectral index  $-0.9$ , affected by internal and external Faraday dispersion for different values of  $\sigma_{\text{RM}}$ , from Arshakian & Beck (2011).



**Figure 2.6:** From Arshakian & Beck (2011): "Polarized intensity for a total-intensity synchrotron emission of spectral index  $-0.9$  and depolarization by internal (solid line) and external (dashed line) Faraday dispersion for different values of  $\sigma_{\text{RM}}$ ".

## 2.4 Rotation Measure Grid

The RMs of the polarized sources are used to build the Rotation Measure grid of the sky, an important resource to investigate the cosmic magnetism at different scales in the Universe (Heald et al. 2020). An RM grid is useful to probe both the Galactic magnetized foreground (e.g. Hutschenreuter & Enßlin 2020) and the extragalactic magnetized Universe (e.g. Vacca et al. 2016).

Early RM grid studies were conducted at 1.4 GHz and contain large systematic uncertainties, due to their poor frequency sampling. Among them, the catalogue drawn up by Taylor et al. (2009), produced from the NRAO VLA Sky Survey (NVSS, Condon et al. (1998)), is the main polarization survey. The catalogue contains RM values for 37 543 lines of sight to polarized radio sources and covers the 82% of the sky north of declination  $-40^\circ$ , finding an average of one polarized source per  $\text{deg}^2$ .

The new generation of telescopes at lower frequencies are mapping the RMs

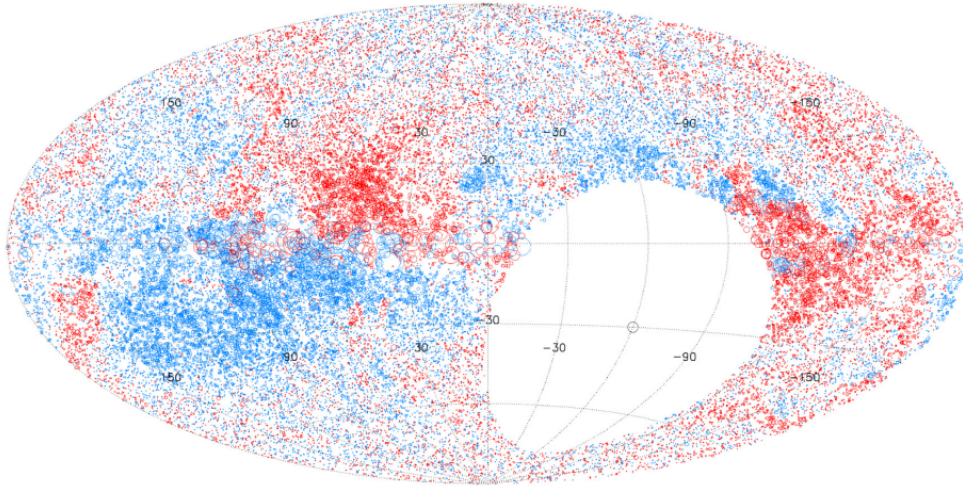


**Figure 2.7:** RM grid at 1.4 GHz. Red circles are positive rotation measures and blue circles are negative. The size of the circle scales linearly with the magnitude of rotation measure. From Taylor et al. (2009).

across the sky with high precision on the inferred RM values through low-frequency broad-band polarimetry. For example, the POLarised GLEAM Survey (POGS) catalogued 517 radio sources covering 25 489 square degrees of sky between Declination  $+30^\circ$  and  $-82^\circ$  in the frequency range of 169 to 231 MHz (Riseley et al. 2020).

At  $\sim 1$  GHz the SKA1-survey will cover a large field of view and, at  $\mu\text{Jy}$  levels, it may provide an RM grid  $\sim 300$ - $1000$  times denser than the RM grid based on the NVSS survey (Govoni et al. 2014).

In the frequency range of 120 to 168 MHz the LOFAR Two-Metre Sky Survey (LoTSS) is mapping the RMs at declinations higher than  $0^\circ$  (O’Sullivan et al. 2023). In addition to these surveys, deepest polarization studies on smaller fields are carrying out, allowing for denser grids (e.g. Neld et al. 2018; Herrera Ruiz et al. 2021 at 120-168 MHz). We will discuss the LoTSS RM grid in more detail in Sec. 4.

In Fig. 2.8 we show a plot from Heald et al. (2020), where RM Grid survey strengths of various existing and future radio surveys are illustrated. We added a point, highlighted in the red box, to show our research work on polarized sources is found in this context, that we will explain in detail in Chapter 5.

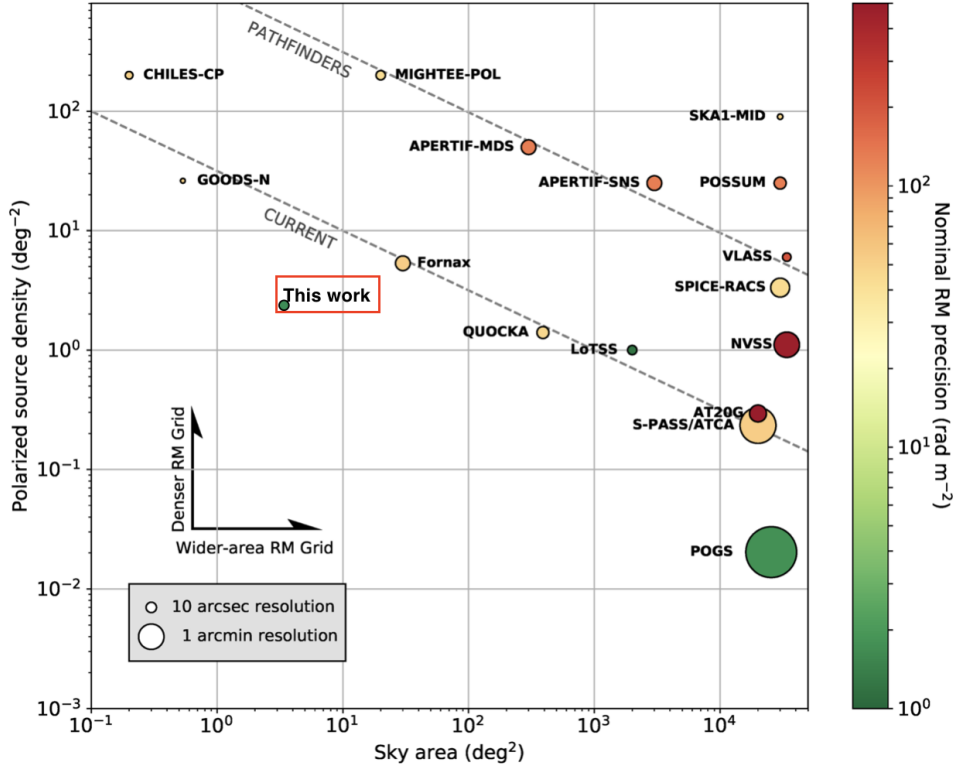


**Figure 2.8:** From Heald et al. (2020): illustration of the RM Grid survey strengths of various existing and future radio surveys. The size of each marker reflects the angular resolution of the survey, and the colour indicates the nominal RM precision that can be reached, where green indicates the capacity for measurements with lower RM uncertainties. Diagonal dashed lines are intended to highlight the locus of “current” (lower) and “pathfinder” (upper) survey capability. We added the point, highlighted in the red box, relative to our work on an area of  $25 \text{ deg}^2$  of the sky centred on the ELAIS-N1 field, discussed in Sec. 5.

Since the RM values are given by an integration along the line of sight, the attribution of optical counterparts and redshifts to the sources that compose the RM grid are of fundamental importance to be able to discern the different contributions to the RM values due to the magnetic fields at different distances.

Some radio source populations in dense magneto-ionic medium are depolarized at long wavelengths but can be observed at shorter wavelengths, then the combination of RM grid catalogs at different radio wavelengths could help

to better understand and discern the different contributions to the Faraday rotation along the line of sight.

## CHAPTER 3

---

### Polarized source counts

---

Source counts of sources detected in total flux density, that we call *total source counts*, and source counts of sources detected in polarized flux density, that we call *polarized source counts* are useful for studying the statistical properties of radio sources. In particular, polarized source counts that consider very low flux density sources (sub-mJy) can be used to predict the number density of RM values that will be produced by future deep polarization surveys with the SKA (Stil et al. 2014; O’Sullivan et al. 2008; Beck & Gaensler 2004), and deep polarized source counts and total source counts combined with models of cosmological evolution of radio sources can provide information on the relation between the cosmic evolution of magnetic field properties and radio source evolution. Furthermore, polarized source counts are an important tool for studies of primordial polarization in the Cosmic Microwave Background (CMB): polarization from extragalactic sources is a contaminant of the polarized signal from the CMB and its contribution to the power spectrum must be estimated and removed (i.e. Tucci & Toffolatti 2012; Puglisi et al. 2018).

Polarized source counts are often calculated starting from the total source counts since, especially at low radio frequencies, the small number of polarized sources is not sufficient for statistical studies.

Most of the studies on this topic have been conducted at 1.4 GHz. Beck & Gaensler (2004) constructed a polarized source counts model starting from data related to polarized sources in NVSS Condon et al. (1998) to predict detection statistics for the SKA RM Survey. Stil et al. (2014) derived the polarized radio source counts from stacked NVSS data, predicting fewer polarized radio sources for future surveys with the Square Kilometre Array and its pathfinders. Also Mesa et al. (2002) and Tucci et al. (2004) used NVSS data to study the fractional polarization distributions for steep- and flat/inverted-spectrum for sources NVSS, finding their distributions to exhibit log-normal form. O’Sullivan et al. (2008) as well modeled polarized sources using data from NVSS and the DRAO ELAIS-N1 deep field survey (Taylor et al. 2007), using a luminosity-dependent model for the polarization of FRI and FRII AGN.

Empirical studies on the polarized source counts at 1.4 GHz were carried out in several projects (Taylor et al. 2007; Grant et al. 2010; Subrahmanyam et al. 2010; Hales et al. 2014; Berger et al. 2021), covering areas of several square degrees. The deepest polarized source counts so far were conducted by Rudnick & Owen (2014) (down to a noise level of  $3 \mu\text{Jy beam}^{-1}$ ), for a small area in the GOODS-N field of approximately  $0.3 \text{ deg}^2$ .

Deeper survey with better sensitivity (lower  $\sigma$ ) and wide field of view help in understanding source counts. Indeed, for instance, an anti-correlation trend between fractional polarization and total flux density of the faint extragalactic radio source population at 1.4 GHz was observed by Mesa et al. (2002), Tucci et al. (2004), Taylor et al. (2007) and Grant et al. (2010), and it was supposed to be dependent on physical properties of the sources. Reaching a better sensitivity, Hales et al. (2014) ( $\sigma \sim 100 \mu\text{Jy beam}^{-1}$ ) and Berger et al. (2021) ( $\sigma \sim 7 \mu\text{Jy beam}^{-1}$ ) found that this relation originates from the incompleteness affecting the faintest sources in the sample. Wider fields of view instead minimize the cosmic variance that may cause differences between the results of small fields.

In the following sections we explain the theory of the source counts following Condon & Ransom (2016) and Condon (1988). We will give the definition of total source counts, but the same way of reasoning applies in the case of polarized source counts, which are the object of our studies and which we will use as examples in figures and tables.

### 3.1 Definition

Statistical samples of the radio-source population are given by radio surveys. Let us consider a radio survey that covers a certain region of the sky  $\Omega$  in unit of, for instance, sr or deg<sup>2</sup>, at frequency  $\nu$  and complete above a flux density  $S_{\text{lim}}$ . We can compute the histogram of the flux density values  $S$  of the sources, in order to see how many sources have a flux density in each bin  $\Delta S$ . Fig. 3.1 shows the histogram of the polarized flux densities of sources detected in a region of 25 deg<sup>2</sup> at 150 MHz in our study (more details in Sec. 5).

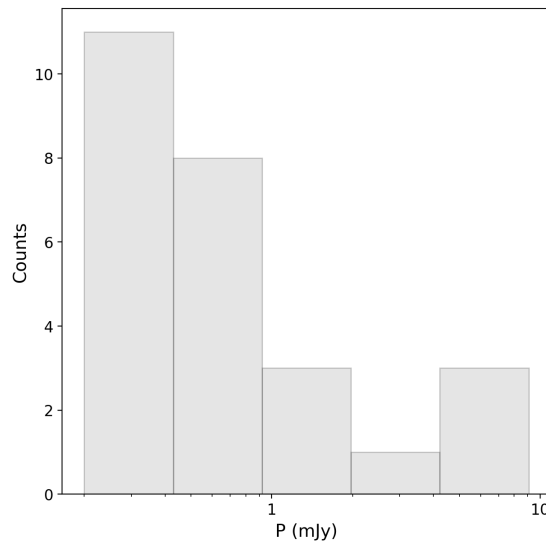


**Figure 3.1:** Histogram of the polarized flux densities for the polarized source detected in the ELAIS-N1 LOFAR deep field (this work).

To facilitate the comparison between results from different surveys, the number of sources is normalized by the area covered by the survey and the width of the polarized flux density bin, hence the commonly seen units of sr<sup>-1</sup>Jy<sup>-1</sup>.

During the normalization by unit of area, we must take into account that our data are primary-beam corrected. The primary beam  $PB$  can be considered as the sensitivity of the interferometer as a function of direction. Primary-beam-corrected images are obtained dividing the image by the primary beam

of the telescope, that is generally described by a Gaussian function:

$$PB(\theta) = \exp \left[ -4 \ln 2 \left( \frac{\theta}{\theta_{\text{FWHM}}} \right)^2 \right] \quad (3.1)$$

where  $\theta_{\text{FWHM}}$  is the full width half-maximum of the Gaussian beam. This corrects the source fluxes, but also increases the noise of the resulting image towards the outskirts of the map. For a Gaussian primary beam, the noise  $\sigma$  varies with the radius  $\theta$  as:

$$\sigma = \frac{\sigma_0}{PB(\theta)} \quad (3.2)$$

where  $\sigma_0$  is the noise at the center of the field. In Fig. 3.2 we show the noise map computed in our work and its noise values as a function of radius, that can be used to infer the shape of the primary beam of our telescope.

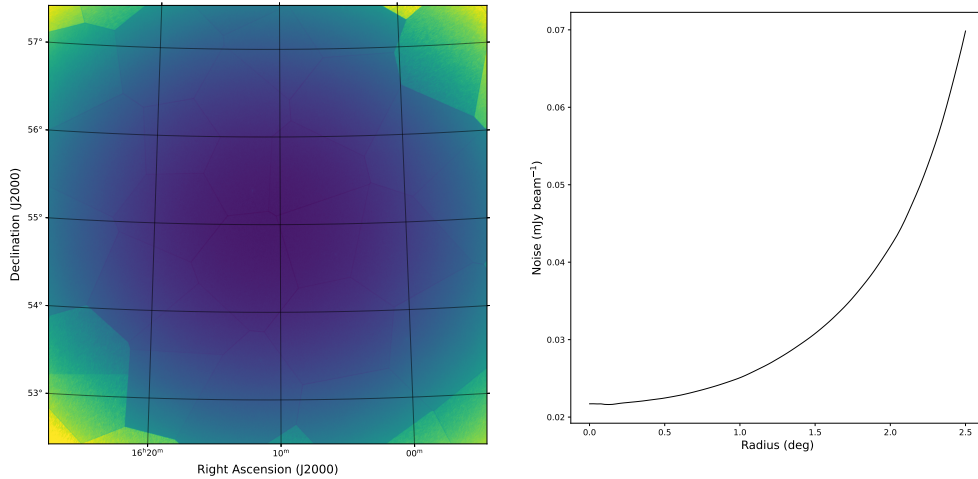


**Figure 3.2:** Left panel: noise map over the field studied in our work. A Gaussian primary beam should lead to noise map where the noise increases with the radius from the center of the field. Here this behavior is visible but not immediately evident due to the data calibration process, which divides the field into facets, distinguishable in the image. Right panel: noise values as a function of radius from the center of the noise map. Here we can see clearly how the noise increases with radius, with trend that suggest the Gaussian shape of the primary beam.

If we combine Eq. 3.1 and Eq. 3.2, we can express the area  $A$  of the image

with noise less than a certain value  $\sigma$  as:

$$A(\text{noise} < \sigma) = \frac{\pi}{4 \ln 2} \theta_{\text{FWHM}}^2 \ln \frac{\sigma}{\sigma_0} \quad (3.3)$$

Imposing a threshold in the signal-to-noise ratio for detection, the effective area  $A_{\text{eff}}$  in which we can actually find a polarized source depends on the noise in the image. Therefore we can detect the faintest polarized sources only in the center of the image. For this reason the number of sources in each bin normalized by unit of area,  $n_{\text{eff}}$ , for example in  $\text{sr}^{-1}$  or  $\text{deg}^{-2}$ , is computed using the effective area  $A_{\text{eff}}$ :

$$n_{\text{eff}} = \frac{N}{A_{\text{eff}}} \quad (3.4)$$

where  $A_{\text{eff}}$  indicates the area where the noise is low enough so that we can detect a source with polarized flux density at a given signal-to-noise ratio.

*Differential number counts*  $n(S)$ , expressed for instance in  $\text{sr}^{-1}\text{Jy}^{-1}$  or  $\text{deg}^{-2}\text{Jy}^{-1}$ , are defined as the number of sources per unit area and per unit of flux density, with flux density between  $S$  and  $S + dS$ :

$$n(S) = \frac{dn_{\text{eff}}}{dS} \quad (3.5)$$

The differential number counts in polarization from our data are shown in Fig. 3.3 and in Table 3.1 we give information.

**Table 3.1:** Differential polarized source counts at 150 MHz, our work.

bin (mJy)	N	Area (deg <sup>2</sup> )
0.200-0.429	11	3.14
0.429-0.920	8	16.61
0.920-1.973	3	22.51
1.973-4.233	1	24.39
4.233-9.079	3	24.96

*Col 1:* Flux density bin range, in mJy; *Col 2:* Number of sources detected in the bin; *Col 3:* Area where the sources with flux density in the bin range are detectable, in deg<sup>2</sup>.

*Cumulative source counts*  $N(\geq S)$  give the distribution of the number of

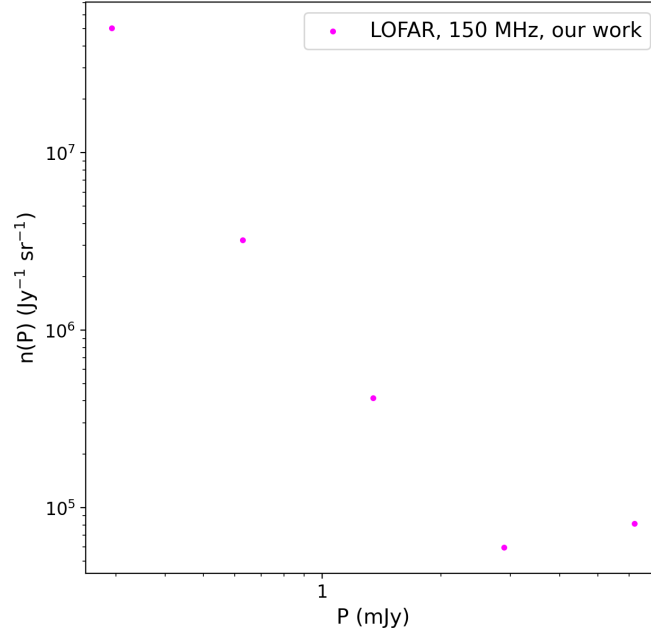


**Figure 3.3:** Differential polarized source counts at 150 MHz, our work.

sources per unit of area brighter than a flux density  $S$ :

$$N(> S) = \int_S^{+\infty} n(S) dS = \int_S^{+\infty} \frac{dN}{dS} dS \quad (3.6)$$

## 3.2 Measurements in total flux density and polarized flux density

Let us consider first the measurements in total flux density.

In a static Euclidean Universe uniformly filled with sources of luminosity  $L$  and number density  $\rho$ , the number of sources  $N$  can be expressed as the product of  $\rho$  and the volume  $V$ . In a spherical volume of radius  $r$ ,  $N$  is:

$$N = \rho V = \rho \frac{4}{3} \pi r^3 \quad (3.7)$$

We can observe only the sources above the flux density limit of our survey, so we are able to observe only the sources within a certain radius  $r$  that depends

on  $L$  and  $S$ , so that  $S > S_{\text{lim}}$ , where:

$$S_{\text{lim}} = \frac{L}{4\pi r_{\text{lim}}^2} \quad (3.8)$$

so that  $r < r_{\text{lim}} = \left(\frac{L}{4\pi S_{\text{lim}}}\right)^{\frac{1}{2}}$

From Eq. 3.7, the number of sources is therefore related to  $S$ :

$$N \propto r^3 \propto S^{-\frac{3}{2}} \quad (3.9)$$

and the differential number  $n(S)$  depends on  $S$  as:

$$n(S) = \frac{dN}{dS} \propto S^{-\frac{5}{2}} \quad (3.10)$$

Plotting the *Euclidean normalized differential source count*  $n(S)S^{\frac{5}{2}}$  as a function of  $S$  should then yield a horizontal line in a static Euclidean Universe. However, the observations at radio frequencies show a different trend, as in Figure 3.4 from Condon (1984) at 1.4 GHz. Indeed, the slope of source counts was studied and used as evidence against the non-evolving, Steady State cosmological models from early radio surveys (i.e. Ryle & Scheuer 1955). The slope of the source counts is determined by the different types of sources that contribute at every flux, that depends on their luminosity function at various redshifts. In Fig. 3.4 the dashed line in the flux density range  $10^{-5} < S < 10^{-2}$  Jy is representative of the star-forming galaxy population; the dashed line in the flux density range  $2.5 \times 10^{-4} < S < 1$  Jy corresponds to the AGN population and the plateau above 1 Jy is related to the local bright radio sources.

Similar slopes in total source counts are found also at 150 MHz, as shown in Figure 3.5, where the normalized source counts from Mandal et al. (2021) are reported.

Euclidean normalized differential source counts are computed also in polarization. In Figure 3.6 we show the total flux density and polarized flux density Euclidean normalized differential source counts at 1.4 GHz from Grant et al. (2010). Models are also shown, which will be discussed in the following section.

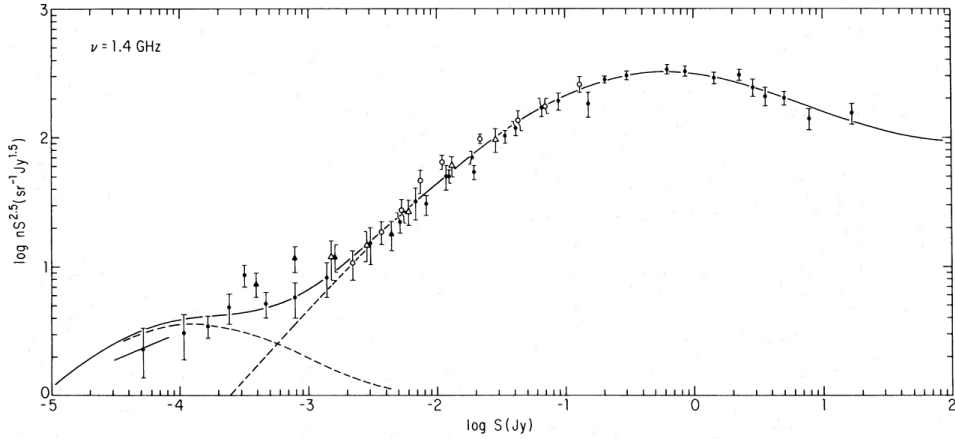


**Figure 3.4:** Euclidean normalized differential source counts in total flux density at 1.4 GHz, from Condon (1984). The dashed line in the flux density range  $10^{-5} < S < 10^{-2}$  Jy represents the star-forming galaxy population; the dashed line in the flux density range  $2.5 \times 10^{-4} < S < 1$  Jy corresponds to the FRI and FRII populations and the plateau above 1 Jy is related to the local bright radio sources.

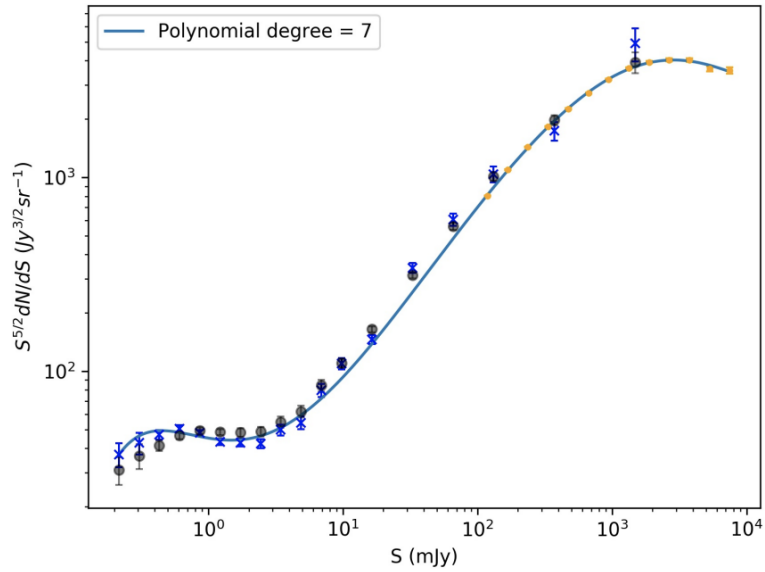


**Figure 3.5:** Euclidean normalized differential source counts for LOFAR deep fields and their best fit in total flux density at 150 MHz, from Mandal et al. (2021).

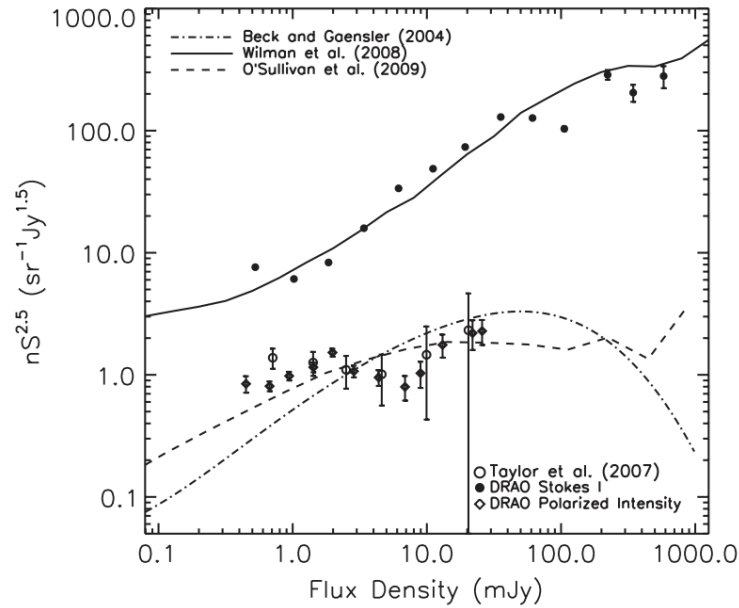


**Figure 3.6:** Euclidean normalized differential source counts at 1.4 GHz, from Grant et al. (2010). The solid line represents source counts in total flux density, the discontinuous lines are modeled polarized source counts.

### 3.3 Modeling source counts in polarization

Polarized source counts can be modeled from the total-intensity source counts and polarization distributions derived from analysis of polarization observations.

The simplest model assumes a constant fractional polarization for the polarized population; then the polarized source counts are made by multiplying the total source counts by a constant fractional polarization (Tucci & Toffolatti 2012; Stil et al. 2014). We show in Figure 3.7 an example of this method from Tucci & Toffolatti (2012), where they used a constant fractional polarization of 3.3% for all the extragalactic sources.

Other models calculate polarized source counts through the convolution of source counts in total flux density with a probability density function.

Tucci & Toffolatti (2012) express the polarization number counts  $n(P)$  as:

$$n(P) = N \int_{S_0}^{\infty} \mathcal{P}(P, S) dS = N \int_{S_0}^{\infty} \mathcal{P}(\Pi, S) \frac{dS}{S} \quad (3.11)$$

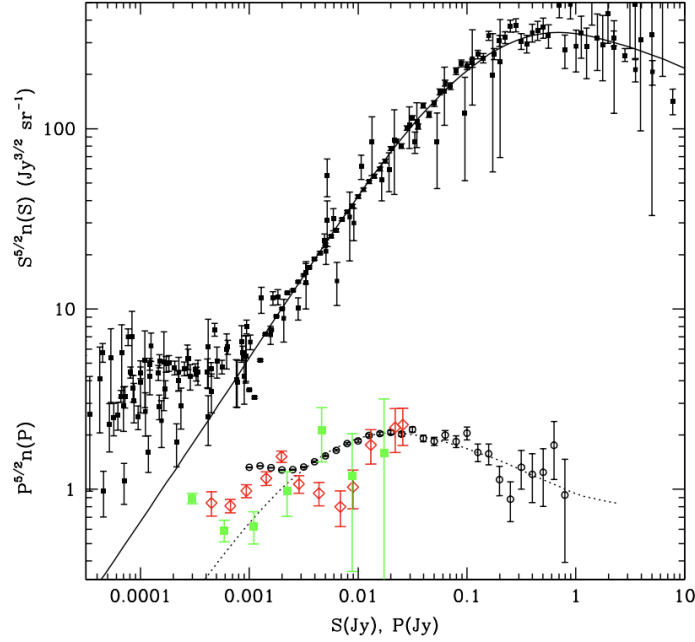


**Figure 3.7:** Euclidean normalized differential source counts at 1.4 GHz, as function of total intensity (upper points) and of polarized intensity (lower points). The dotted line, that represents the polarized source counts, is obtained by the counts in total intensity (solid line) and assuming a constant fractional polarization of 3.3% for all the extragalactic sources. From Tucci & Toffolatti (2012).

where  $N$  is the total number of sources with  $S \leq S_0$  in the sample,  $\mathcal{P}(P, S)$  and  $\mathcal{P}(\Pi, S)$  are the probability functions of observing a polarized intensity  $P$  and a fractional polarization  $\Pi$  in a source of flux density  $S$ . Assuming  $\Pi$  independent of  $S$ ,  $n(P)$  can be derived as:

$$n(P) = \int_{S_0}^{\infty} \mathcal{P}\left(\Pi = \frac{P}{S}\right) n(S) \frac{dS}{S} \quad (3.12)$$

where  $n(S)$  is the density of number of sources per unit of polarized flux density bin. The probability function  $\mathcal{P}(\Pi)$  is modeled by a log-normal distribution:

$$\mathcal{P}(\Pi) = \frac{1}{\sqrt{2\pi}\sigma\Pi} \exp\left\{-[\log(\Pi/\Pi_{\text{med}})]^2/2\sigma^2\right\} \quad (3.13)$$

where  $\Pi_{\text{med}}$  and  $\sigma$  are the median and the scale parameter of the distribution, respectively. The reason for this distribution is due to the work of Mesa et al. (2002), where it is shown that the distribution of the number of sources with flux densities  $>80$  mJy as a function of the fractional polarization in NVSS data can be approximated with a log-normal function, both for steep- and flat-spectrum sources.



# CHAPTER 4

---

## Polarization with LOFAR

---

### 4.1 LOFAR

LOFAR, the LOw-Frequency ARray, is a new-generation radio interferometer built in the north of the Netherlands and across Europe. Utilizing a novel phased-array design, LOFAR covers the largely unexplored low-frequency range from 10–240 MHz. LOFAR allows for measurements of the Stokes parameters  $I$ , at resolution of 6 arcsec, and  $Q$ ,  $U$ ,  $V$ , at resolution of 3 arcmin and 20 arcsec, using a large number of channels across the observational bandwidth. These channels allow for measurements of the linearly polarized emission and of the Faraday rotation. Measuring weak magnetic fields ( $\mu\text{Jy}$ ) in intergalactic space is difficult, but LOFAR provides the ability to measure the Faraday rotation effect of these weak fields with unprecedented accuracy.

LOFAR is the largest radio interferometer operating at the lowest frequencies that can be observed from Earth. It uses almost 20 000 small antennas, located mainly in the Netherlands; other stations are in Germany, Poland, France, Ireland, Latvia, Sweden, and the United Kingdom; a station in Italy is funded to be built soon. More countries are considering to join as well <sup>1</sup>.

---

<sup>1</sup><https://www.astron.nl/telescopes/lofar>

LOFAR can observe the sky with two types of antennas: Low Band Antenna (LBA), from 10 to 90 MHz, and High Band Antenna (HBA), from 110 to 250 MHz, with a large number of frequency channels across the observational bandwidth.

Radio observations with LOFAR are making possible several fundamental studies of the Universe. The LOFAR community is currently organized into Key Science Projects (KSP) which aim to study phenomena closest to us, starting from the Sun, up to the investigation of the early universe (redshift  $z = 6$  to 11.4), at the epoch of reionization.



**Figure 4.1:** The LOFAR station in the Netherlands. Credits: <https://www.astron.nl/>.

The LOFAR community is working also to produce the LOFAR Two-metre Sky Survey (LoTSS) (Shimwell et al. 2017, 2019, 2022), a deep 120-168 MHz imaging survey that will eventually cover the entire northern sky. 3170 LOFAR pointings will be observed for 8 h, which, at most declinations, is sufficient to produce 6 arcsec resolution images with a sensitivity of  $100 \mu\text{Jy beam}^{-1}$  and accomplish the main scientific aims of the survey, which are to explore the formation and evolution of massive black holes, galaxies, clusters of galaxies and large-scale structure. In comparison to higher frequencies, the LoTSS will match the high resolution achieved by Faint Images of the Radio Sky at Twenty-Centimeters (FIRST; Becker et al. 1995) but over a wider area and, for a typical radio source of spectral index  $\alpha \sim -0.7$ , it will be seven times more sensitive. Similarly, the LoTSS will be 20 times more sensitive to typical radio sources than the lower resolution NRAO VLA Sky Survey (NVSS; Condon et al. 1998). We show these comparisons in Fig. 4.2.

The LoTSS-data release 1 (LoTSS-DR1) Shimwell et al. (2019) covers 2% of the northern sky, for which a catalogue of more than 325 000 sources is derived from Stokes  $I$  continuum maps. The Stokes  $I$  continuum maps at

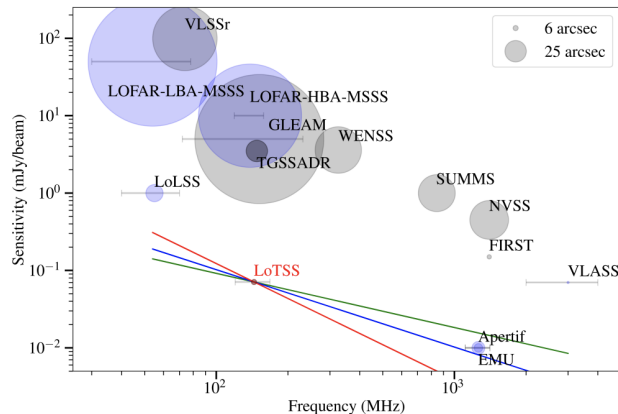


**Figure 4.2:** Image rms, frequency, and angular resolution (linearly proportional to the radius of the markers) of LoTSS-data release 1 (LoTSS-DR1) in comparison to a selection of existing wide-area completed (grey) and upcoming (blue) radio surveys. The horizontal lines show the frequency coverage for surveys with large fractional bandwidths. The green, blue, and red lines show an equivalent sensitivity to LoTSS for compact radio sources with spectral indices of  $\sim -0.7$ ,  $\sim -1.0$ , and  $\sim -1.5$ , respectively. From Shimwell et al. (2019).

6 arcsec-resolution have a sensitivity better than  $0.1 \text{ mJy beam}^{-1}$ . LoTSS-DR1 includes optical counterparts for 71% of the radio sources (Williams et al. 2019) and photometric redshifts for these sources (Duncan et al. 2019). The last data release from LoTSS, the LoTSS-DR2 (Shimwell et al. 2022), covers the 27% of the northern sky, that results in a catalog of more than 4 millions radio sources. The Stokes  $I$  continuum maps at 6 arcsec-resolution have a median rms sensitivity of  $83 \mu\text{Jy beam}^{-1}$ . The LOFAR community, together with other astronomers and non-astronomers who were involved through the "LOFAR galaxy zoo" project, worked to find the host galaxies of the LoTSS-DR2 catalog, of which 84% have an optical ID candidate and 57% have a spectroscopic or photometric redshift estimate (Hardcastle et al., in prep.).

The LOFAR community is working also to produce the LOFAR LBA Sky Survey (LoLSS) to cover the entire northern sky with 3170 pointings in the frequency range between 42–66 MHz, at a resolution of 15 arcsec and at a sensitivity of  $1 \text{ mJy beam}^{-1}$  (de Gasperin et al. 2021).

The LoTSS is complemented by a few deeper fields, known as the LoTSS-Deep Fields (Sabater et al. 2021; Tasse et al. 2021). The deep fields include

the Bootes, Lockman Hole, and European Large Area Infrared Space Observatory Survey- North 1 (ELAIS-N1) fields. These fields have a multiwavelength coverage and are ideal to probe a new fainter population of radio sources and study the unknown polarized radio source population at sub-mJy flux densities at low frequencies.

## 4.2 Constrain cosmic magnetic fields with LOFAR

As mentioned earlier, cosmic magnetic fields at radio wavelengths can be studied indirectly by the Faraday rotation of polarized background emission due to magnetic media along the line of sight. However, investigation of linear polarization at these frequencies is complicated by the effects of wavelength-dependent depolarization. Furthermore, ionospheric Faraday rotation (Sotomayor-Beltran et al. 2013), instrumental polarization, uncertainty in the primary-beam model made polarization studies challenging with LOFAR. Calibration and imaging at high resolution ( $\leq 1$  arcmin) is difficult at low frequencies, so beam depolarization can often be a limitation. Despite these difficulties, polarization studies are possible as the nature of the data and the characteristics of the instrument become better understood. In Fig. 4.3 we show the RMTF for LOFAR in HBA configuration with 640 equally spaced frequency channels in the range from 114.9 to 177.4 MHz. This permits to reach a resolution in Faraday depth of  $0.9 \text{ rad m}^{-2}$ , a maximum observable Faraday depth of  $300 \text{ rad m}^{-2}$ , and the largest scale in  $\phi$  space to which the data are sensitive is  $1.07 \text{ rad m}^{-2}$ .

LOFAR has the potential to minimize the effect of beam depolarization with observations at higher angular resolution. Van Eck et al. (2018) reported developments in polarization processing for the 570  $\text{deg}^2$  preliminary data release region from the LoTSS (Shimwell et al. 2017, 2019), finding 0.16 polarized radio sources per square degree at 150 MHz with resolution of 4.3 arcmin and sensitivity of  $1 \text{ mJy beam}^{-1}$  root mean square (rms). Neld et al. (2018) developed a computationally efficient and rigorously defined algorithm to find linearly polarized sources in LOFAR data and applied it to previously calibrated data of the M51 field (Mulcahy et al. 2014); they found at 150 MHz 0.3 polarized sources per square degree, at resolution of 20 arcsec and rms of  $100 \mu\text{Jy}/\text{beam}$ . O’Sullivan et al. (2019) presented the Faraday RM and

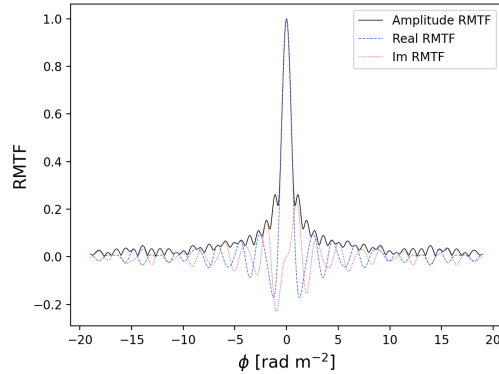


**Figure 4.3:** LOFAR RMTF in HBA configuration with 640 equally spaced frequency channels in the range from 114.9 to 177.4 MHz.

depolarization properties of a giant radio galaxy using LOFAR, demonstrating the potential of LOFAR to probe the weak signature of the intergalactic magnetic field (see also O’Sullivan et al. 2020; Stuardi et al. 2020; Mahatma et al. 2019, 2021).

Herrera Ruiz et al. (2021) worked on the ELAIS-N1 field, developed a new algorithm to stack different observation epochs in polarization, finding 10 polarized sources in 16 deg<sup>2</sup> at resolution of 20 arcsec in Stokes  $Q, U$  data cube.

From the LoTSS-DR2, a catalog of more than 2 500 high-precision ( $\sim 1$  rad m<sup>-2</sup>) RM values from extragalactic polarized sources over 5 720 deg<sup>2</sup> was produced, for a number density of 0.43 polarized sources per square degree. The linear polarization and RM properties of the sources were derived from image at 20 arcsec-resolution. The catalog contains the host galaxy identification for 88% of the sources, along with redshifts for 79%, both photometric and spectroscopic (O’Sullivan et al. 2023).

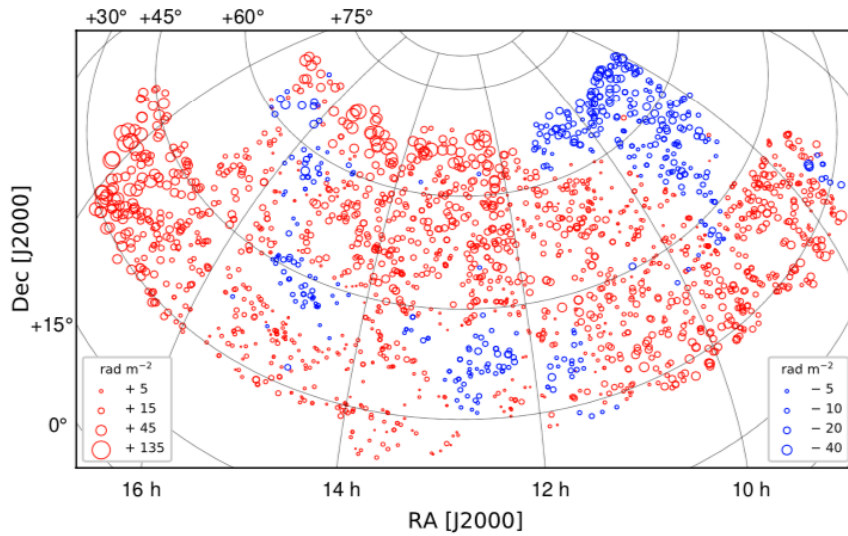


**Figure 4.4:** From O’Sullivan et al. 2023: "Sky distribution of the polarized sources across the LoTSS-DR2 13 hr field, in equatorial coordinates and with an orthographic projection. The red/blue coloured circles correspond to positive/negative RM values, and the size of the circles are proportional to the magnitude of the RM (as quantified in the figure legends). There are 2 039 sources in the RA=13 hr field, which corresponds to an areal number density of  $0.48 \text{ deg}^{-2}$ ".

---

## Polarization in the ELAIS-N1 LOFAR Deep Field

---

### **5.1 The European Large-Area ISO Survey-North 1 (ELAIS-N1)**

The ELAIS-N1 field is a region of the Northern Hemisphere (centred on RA = 16h10m01s, Dec = 54°30m360s) observed by the ELAIS survey (Oliver et al. 2000), originally chosen for deep extragalactic observations with the Infrared Space Observatory (ISO) because of its low infrared background (Rowan-Robinson et al. 2004; Vaccari et al. 2005). The ELAIS-N1 field has an ample multiwavelength coverage, of which a detailed description can be found in Kondapally et al. (2021).

At radio frequencies, this region has been covered by several radio surveys as the Westerbork Northern Sky Survey (WENSS, 325 MHz, Rengelink et al. 1997), the NRAO Very Large Array Sky Survey (NVSS, 1.4 GHz, Condon et al. 1998), and the Faint Images of the Radio Sky at Twenty Centimeters Survey (FIRST, 1.4 GHz, Becker et al. 1995; White et al. 1997). The ELAIS-N1 field has also been observed with the Giant Metrewave Radio Telescope (GMRT) at 325 MHz (Sirothia et al. 2009), at 610 MHz (Ocran et al. 2020)

and with the upgraded GMRT at 300-500 MHz (Chakraborty et al. 2020). Deep field observations in total intensity with the LOw Frequency ARray (LOFAR) at 115-177 MHz have recently been examined by Sabater et al. (2021). Studies on the polarization of radio sources in ELAIS-N1 at 1.4 GHz were conducted by Taylor et al. (2007) and Grant et al. (2010). Taylor et al. (2007) imaged a region of  $7.43 \text{ deg}^2$  to a maximum sensitivity in Stokes  $Q, U$  of  $78 \mu\text{Jy beam}^{-1}$ , detecting about 11 polarized sources per square degree. Grant et al. (2010) imaged a region of  $15.16 \text{ deg}^2$ , to a maximum sensitivity in Stokes  $Q, U$  of  $45 \mu\text{Jy beam}^{-1}$ , and detected about 9 sources per square degree. They constructed also the Euclidean-normalized polarized differential source counts down to  $400 \mu\text{Jy}$  and found that fainter radio sources have a higher fractional polarization than the brighter ones.

## 5.2 The ELAIS-N1 LOFAR Deep Field

The ELAIS-N1 LOFAR Deep Field is the deepest of the LoTSS deep fields to date. At frequency of 114.9-177.4 MHz, it was observed for an effective observing time of 163.7 h, reaching a root mean square noise level of  $20 \mu\text{Jy beam}^{-1}$  in the central region and below  $30 \mu\text{Jy beam}^{-1}$  in the internal 10 square degrees in the Stokes I image at 6 arcsec resolution. More than 80 000 radio sources were detected in the full area of 68 square degrees. The source associations, cross-identifications, and multi-wavelength properties of the faint radio source population detected in the central  $\sim 7.15 \text{ deg}^2$  were performed by Kondapally et al. (2021) for more than 31 000 sources. A photometric and spectroscopic catalog for more than 2 100 000 sources is also available Duncan et al. (2021).

The ELAIS-N1 LOFAR Deep Field was studied in polarization by Herrera Ruiz et al. (2021) and Šnidarič et al. (submitted). Herrera Ruiz et al. (2021) combined 6 8-hours observation epochs for an area of  $16 \text{ deg}^2$ , finding about 0.6 polarized sources per square degree at resolution of 20 arcsec and reaching the lower sensitivity of  $26 \mu\text{Jy beam}^{-1}$  in the central area. Šnidarič et al. (submitted) combined 20 eight-hour-long observation epochs for an area of  $\sim 36 \text{ deg}^2$  at 4.3 arcmin-resolution to detect faint component of diffuse Galactic polarized emission, not clearly visible in a single observation.

We developed and used the stacking technique to be able to see the faintest polarized sources and improve the number density of the RM grid at 150 MHz.

The method allowed us to go from 5 sources, detected in a single epoch (i.e. 0.2 polarized source per square degree), to 32 sources after stacking 19 epochs (i.e. 1.28 polarized sources per square degree.) In Fig. 5.1 we show the Faraday rotation measure grid of the ELAIS-N1 LOFAR Deep field produced in our work.

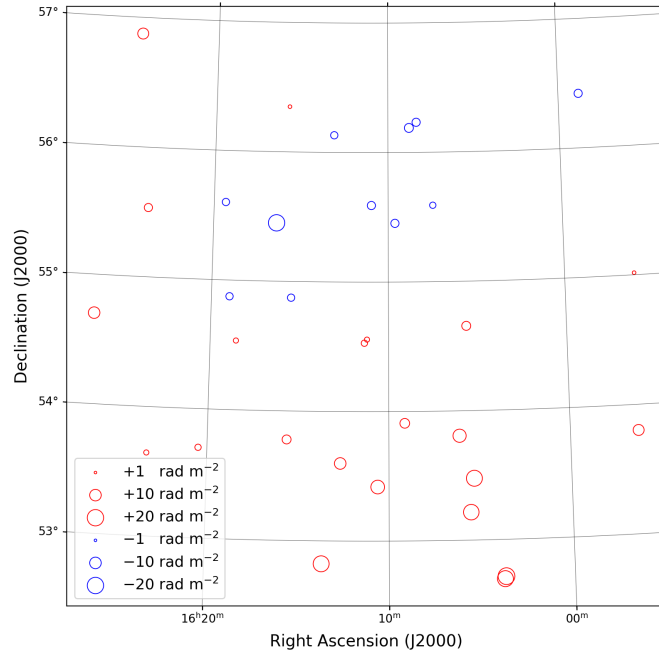


**Figure 5.1:** RM grid derived in our work on the ELAIS-N1 LOFAR Deep Field. By stacking 19 epochs at 6 arcsec resolution, we found 32 polarized sources in  $25 \text{ deg}^2$ , namely 1.28 polarized sources per square degree and 2.7 times the number density found by O’Sullivan et al. (2023) in the LoTSS-DR2 at 20 arcsec resolution. The red/blue coloured circles correspond to positive/negative RM values, and the size of the circles are proportional to the magnitude of the RM.

## 5.3 Observations

The ELAIS-N1 LOFAR Deep Field was observed in the observation cycles 0, 2, and 4 (proposals LC0\_019, LC2\_024, and, LC4\_008 respectively) from May 2013 to August 2015. The data observed in early LOFAR cycles (0 and 2) were taken jointly with the LOFAR Epoch of Reionization Key Science

Project team, as a potential field for EoR studies (Jelić et al. 2014). The observing configuration of cycle 0 and 2 was different from the standard LoTSS configuration. The observations of the ELAIS-N1 field were taken with the LOFAR high band antennas with a frequency ranging from 114.9 to 177.4 MHz and phase centre of the field in RA = 16h10m01s, Dec = 54°30m36s (J2000). Table 5.1 shows the LOFAR observing configurations for the cycles we used.

**Table 5.1:** LOFAR observing configurations for the ELAIS-N1 deep field and parameters of RM synthesis.

LOFAR cycle	Frequency range [MHz]	Number of frequency channels	Channel width [Hz]
2	114.979 - 177.401	800	78125.00
4	114.989 - 177.391	640	97656.25

Observations from cycle 2 and cycles 4 contains 22 8-hour-long epochs. They were imaged at 6 arcsec-resolution in Stokes Q and U frequency cubes, covering an area of 25 deg<sup>2</sup>. Of these, five cubes did not contain all the expected frequency channels. We reconstructed two cubes, so it was possible to identify the missing channels thanks to the file produced during processing, and we had to exclude three cubes from the analysis because it was not possible to identify the missing channels. The 19 observations and datasets used are summarized in Table 5.2.

## 5.4 Stacking polarization data

As seen in the previous sections, it is difficult to detect polarized emission at low radio frequencies, and this is particularly arduous for very faint sources, where the polarized signal can have value close to the noise  $\sigma$ .

Stacking is a method that can improve of the signal-to-noise ratio through averaging several observational epochs of the same target field.

## Noise

### Gaussian noise

If the noise in an epoch,  $\sigma_i$ , is Gaussian, stacking  $N$  epochs leads to a final noise  $\sigma_{\text{fin}}$  given by:

$$\frac{1}{\sigma_{\text{fin}}^2} = \sum_i^N \frac{1}{\sigma_i^2} \quad (5.1)$$

If the noise has same value  $\sigma$  for all the epochs, the signal-to-noise ratio improves by a factor  $\sqrt{N}$ , allowing to reveal polarized signal not detectable before.

The distribution of the Stokes  $Q, U$  values in frequency cubes is known to be Gaussian. Fig. 5.2 shows the histograms of Stokes  $Q, U$  values for the central region of our field, where we don't detected polarization, and at frequency  $\nu=114.979$  MHz. The dashed line represent the Gaussian drawn with the mean and standard deviation of the distribution.

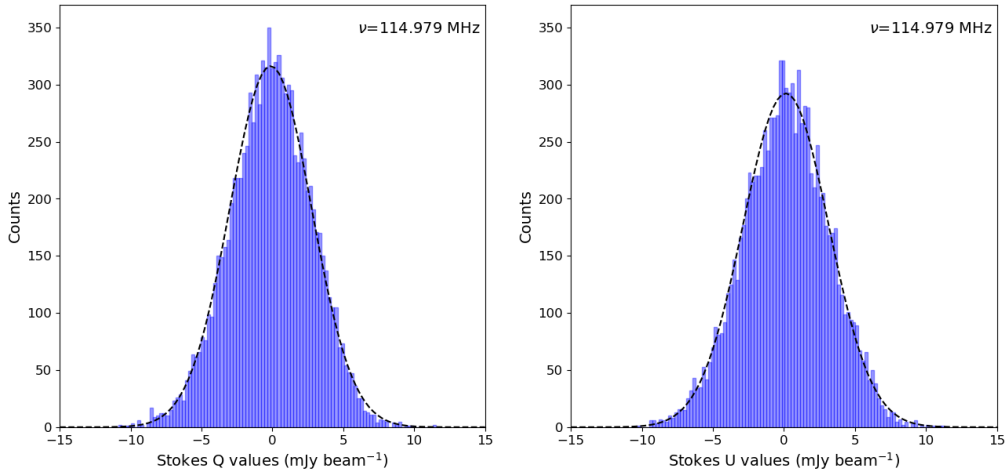


**Figure 5.2:** Example of histogram of the Stokes  $Q$  (left panel) and  $U$  (right panel) values in a frequency cube of our data in one channel at frequency of 114.979 MHz, for the central region of our field of size  $2.5 \times 2.5$  arcmin<sup>2</sup>, where we don't detect a polarized signal. The dashed lines represent the Gaussians drawn with the mean and standard deviation of the distributions. The Gaussian distribution of the  $Q$  values has mean  $\mu_Q = -0.12$  mJy beam<sup>-1</sup> and standard deviation  $\sigma_Q = 2.9$  mJy beam<sup>-1</sup>, the Gaussian distribution of the  $U$  values has  $\mu_U = 0.13$  mJy beam<sup>-1</sup> and  $\sigma_U = 3.0$  mJy beam<sup>-1</sup>.

By transforming from the frequency space to the Faraday depth space via RM synthesis, we expect the noise in the Stokes  $Q(\phi)$ ,  $U(\phi)$  cubes to remain Gaussian. Fig. 5.3 shows the histograms of Stokes  $Q, U$  values for the central region of our data, where we don't detected polarization, in the region  $350 \leq |\phi| \leq 450 \text{ rad m}^{-2}$ , where we don't expect to find a polarized signal. The dashed line represents the Gaussian drawn with the mean and standard deviation of the distribution.

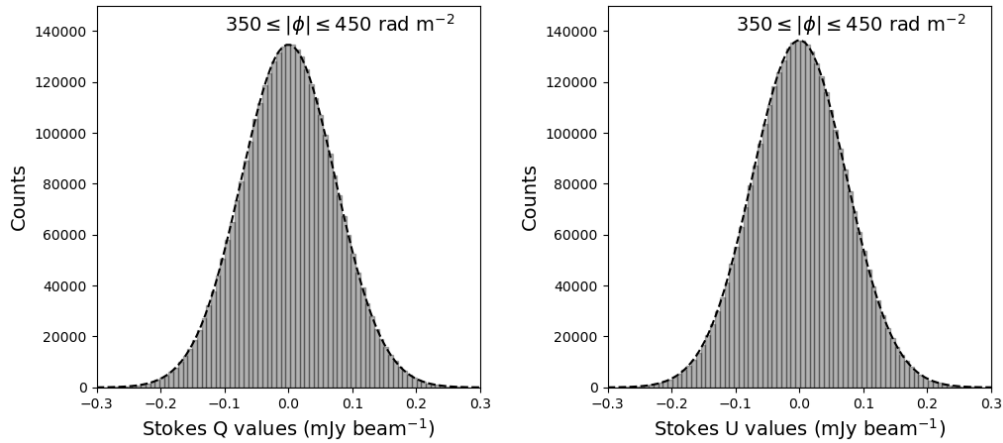


**Figure 5.3:** Example of histogram of the noise in the Stokes parameters as function of  $\phi$  of our data. Left panel refers to the noise in the Stokes  $Q$  parameter and the right panel refers to the noise in the Stokes  $U$  parameter, both in the range  $350 \leq |\phi| \leq 450 \text{ rad m}^{-2}$ , where we do not expect to find a polarized signal, for the central region of our field of size  $2.5 \times 2.5 \text{ arcmin}^2$  with no polarized signal. The dashed lines represent the Gaussians drawn with the mean and standard deviation of the distributions. The Gaussian distributions of the  $Q$  and  $U$  values have, respectively, means of  $\mu_Q = -54 \mu\text{Jy beam}^{-1}$  and  $\mu_U = 31 \mu\text{Jy beam}^{-1}$ ; both distributions have standard deviation of  $\sigma_Q = \sigma_U = 74 \mu\text{Jy beam}^{-1}$ .

### Ricean noise

Following Eq. 2.2, the polarized intensity  $P$  can be written as  $P = \sqrt{Q^2 + U^2}$ , and in Faraday space we can make explicit the dependence on the Faraday depth  $\phi$  and write the Faraday spectrum  $F(\phi)$  as the square root of the sum

of squares of  $Q(\phi)$  and  $U(\phi)$ :

$$F(\phi) = \sqrt{Q^2(\phi) + U^2(\phi)} \quad (5.2)$$

therefore  $F(\phi)$  is described by the Ricean distribution (e.g. Kobayashi 2012) if the Stokes  $Q, U$  parameters are Gaussianly distributed.

Using  $\mathcal{N}$  to indicate a Gaussian distribution, if the Stokes  $Q, U$  parameters are described by  $\mathcal{N}(\mu_Q, \sigma^2)$  and  $\mathcal{N}(\mu_U, \sigma^2)$ , respectively, with  $\mu$  mean and  $\sigma$  standard deviation of the distributions, the complex Faraday spectrum can be written as:

$$\mathcal{F}(\mu, \sigma) = \mathcal{N}(\mu_Q, \sigma^2) + i\mathcal{N}(\mu_U, \sigma^2) \quad (5.3)$$

where  $i$  is the imaginary unit, and the probability density function of Ricean distribution is:

$$f(x|\mu, \sigma) = \frac{x}{\sigma^2} e^{-\frac{x^2 + \mu^2}{2\sigma^2}} I_0\left(\frac{\mu x}{\sigma^2}\right) \epsilon(x) \quad (5.4)$$

where  $\mu = \sqrt{\mu_Q^2 + \mu_U^2}$ ,  $\epsilon(x)$  is unit step Heaviside function and  $I_0$  is the 0th order modified Bessel function of the first kind:

$$I_0(y) = \frac{1}{\pi} \int_0^\pi e^{y \cos \psi} d\psi \quad (5.5)$$

In Fig. 5.4 we show the histogram of the noise values of an example of Faraday cube  $F(\phi)$  computed following Eq. 5.2. The statistics of the noise follows the Ricean distribution.

Because of the definition of  $F(\phi)$  in Eq. 5.2, this quantity is always positive and this over-estimation is known as Ricean bias. A good estimation of the true  $F(\phi)$ ,  $F_{\text{true}}$ , was the subject of the study of George et al. (2012), that found, through simulations:

$$F_{\text{true}} = \sqrt{F_{\text{meas}}^2 - 2.3\sigma_{QU}^2} \quad (5.6)$$

where  $F_{\text{meas}}$  is the measured value of  $F(\phi)$  and  $\sigma_{QU}$  is the error computed from  $Q(\phi)$  and  $U(\phi)$ . We compute the value  $\sigma_{QU}$  as:

$$\sigma_{QU} = \frac{\sigma_Q + \sigma_U}{2} \quad (5.7)$$

where  $\sigma_Q$  and  $\sigma_U$  are computed as the standard deviation of  $Q(\phi)$  and  $U(\phi)$

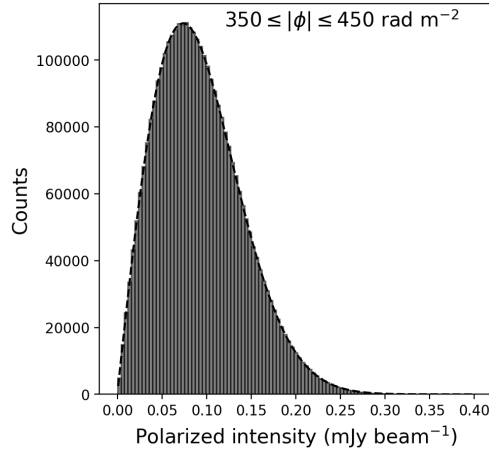


**Figure 5.4:** Example of histogram of the noise in the Faraday cube as function of  $\phi$  of our data,  $F(\phi)$ .  $F(\phi)$  is computed from Eq. 5.2, in the range  $350 \leq |\phi| \leq 450 \text{ rad m}^{-2}$ , where we don't expect to find a polarized signal, for the central region of our field of size  $2.5 \times 2.5 \text{ arcmin}^2$  with no polarized signal. The dashed lines represent the Ricean distribution drawn with mean computed as  $\sqrt{\mu_Q^2 + \mu_U^2} = 62 \text{ } \mu\text{Jy beam}^{-1}$ , and standard deviation computed as  $(\sigma_Q + \sigma_U)/2 = 74 \text{ } \mu\text{Jy beam}^{-1}$ .

from a region where we do not expect to see a real signal (we note that in our data the noise levels in Q and U are very similar).

## The stacking method

The total electron content of plasma in the Earth's ionosphere and the geomagnetic field interact with the polarized radiation coming from the sources under examination, causing a ionospheric Faraday rotation which results as a time- and direction-dependent propagation effect (Murray & Hargreaves 1954; Hatanaka 1956). The value of RM due to this effect is  $0.52 \text{ rad m}^{-2}$  (Sotomayor-Beltran et al. 2013; Jelić et al. 2014, 2015). The LOFAR observations are usually corrected for the ionospheric Faraday rotation, but systematic uncertainties related to ionospheric Faraday rotation corrections or due the dependent calibration can strongly affect RM measurements: a wrong measure in RM of  $\sim 0.8 \text{ rad m}^{-2}$  at LOFAR observational wavelengths (150 MHz) results in a polarization vector rotated of  $180^\circ$ , i.e. fully depolarized.

Herrera Ruiz et al. (2021) showed that that possible changes in the polarization angle  $\chi$  from different observing runs may are present. Indeed, for 6

studied observational epochs of ELAIS-N1, the observed Faraday depth of the bright reference source in each observation had a difference that could vary from 0.12 to +0.05 rad m<sup>-2</sup>.

Therefore, a stacking method needs to take account of these changes in  $\chi$ , in order to avoid to depolarize the signals when combining the epochs and it is crucial to align the polarization angles before stacking.

The key idea is to choose a reference source in a reference epoch as calibrator, determine the polarization angle of the calibrator and the correction to apply to the polarization angle of the reference source in the epoch to be corrected in order to align it with the calibrator, and apply this difference to each polarization angle of the frequency cubes.

After the alignment, we stacked observational epochs belonging to 2 different cycles, with then 2 different setups in the number of frequency channels.

### Reference epoch and reference source

We can evaluate the quality of the epoch through the study of the behavior of the noise. For each epoch, we computed the noise as the standard deviation in the central region of our field, where we know there is no polarized emission, of the Stokes  $Q, U$  frequency channels. We show in Fig. 5.5 the behavior of the noise for epoch 014 (Cycle 2), that we selected as reference epoch as it has the lowest mean value of the noise and fewer spikes in the plot. The spikes correspond to flagged channels for radio-frequency interference (RFI). We chose the reference source used by Herrera Ruiz et al. (2021) as reference source for our work, as it is the brightest source in signal-to-noise ratio closer to the center of the field.

### Stacking in frequency space

We used the stacking method developed by Herrera Ruiz et al. (2021). It is based on the use of a polarized reference source in a reference epoch as polarization angle calibrator on the angles determined through the coherent addition of the signal across the full band using RM synthesis.

Therefore, for each epoch we computed the polarization angle of the reference source and the relative difference with the polarization angle of the calibrator after RM synthesis, and we apply this difference to the entire Stokes  $Q, U$  frequency cubes of epoch to be corrected. This results into the shift of

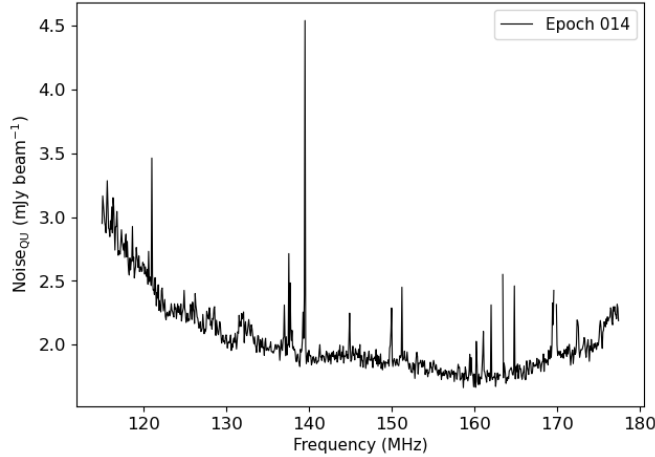


**Figure 5.5:** Noise level of Stokes  $Q$  and  $U$  intensity parameters for epoch 014, the reference epoch, as a function of frequency.

the polarization angle of the epoch to be corrected, in order to have the same vertical intercept as the reference polarization angle. In Fig. 5.6 we show how the method works. On left panels we have the polarization angle in function of the squared wavelength of the calibrator, in black, and of the epoch we want to correct, in cyan. The slope of the curve, so the RM, in almost equal, but the vertical intercept is shifted. On the middle panel we show the polarization angle in function of the squared wavelength of the epoch we want to correct before, in cyan, and after the correction, in blue. We see we are not varying the RM but the curve is shifted upward. On the right panel we have the polarization angle in function of the squared wavelength for of the calibrator and of the epoch corrected. The two curves show now the same vertical intercept.

We want to emphasize that we are correcting only the intercept and not the slope, as RM is the measure we want to determine and we don't know its true value.

Recently, new stacking methods have been proposed, as in Šnidarić et al. (submitted), where they stacked 21 observational epochs of ELAIS-N1 at 4 arcmin resolution through the cross-correlation between observations as a function of the lag in Faraday depth.

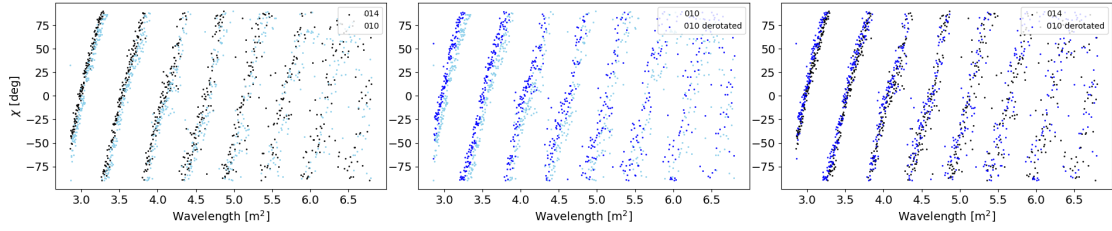


**Figure 5.6:** Polarization angle, in degrees, in function of the wavelength, in  $\text{m}^2$ , for the reference source in the reference epoch (014), in epoch 010 and in epoch 010 after the alignment (i.e. de-rotated epoch).

### Stacking in Faraday depth space

The stacking of Stokes  $Q, U$  frequency cubes with different number of frequency channels result not ideal to be done in frequency space. Herrera Ruiz et al. (2021) showed that the application of the polarization angle correction using an average angle difference across a broad range of frequencies by calculating the slope of the polarization angle as a function of  $\lambda^2$  of one frequency subband, or even individual  $Q, U$  values per channel, causes depolarization of the signal. This is due to the channel-dependency of noise and/or artifacts, to which the polarization angle is sensitive, furthermore the shift in the polarization angle depends on the frequency range chosen.

For these reasons we stacked epochs belonging to the same observing cycle in frequency space, and we combined the two stacked cycle in Faraday depth space. Because of the properties of the noise described in Sec. 5.4, we combined the Stokes cubes  $Q(\phi)$  and  $U(\phi)$  and we computed the Faraday spectrum  $F(\phi)$  following Eq. 5.2.

### Manage big data

We imaged Stokes  $Q, U$  frequency cube at 6-arcsec resolution for an area of  $25 \text{ deg}^2$ . The pixel size in RA-Dec is 1.5 arcsec. This results in a single Stokes parameters frequency cube of  $12005 \times 12005$  pixels for each frequency channels, therefore in  $1.8$  or  $2.3 \times 10^{11}$  pixels depending on whether the number of frequency channels is 640 or 800 (belonging to Cycle 4 or Cycle 2, respectively), and the relative memory size is 800 GB. Considering that for each of the 19 epochs used we made two Stokes frequency cube parameters, we needed to

storage almost 30.4 TB of data in our computers. The RM synthesis can produce several RM cubes where the size of each is almost three times the initial size of the Stokes  $Q, U$  frequency cube.

This enormous amount of data is among the problems connected to LOFAR: the management of the so-called big data. The analysis of LOFAR data in fact requires the use of powerful computers that can manage the calibration and analysis of large amounts of information.

The Stokes  $Q, U$  frequency cubes were processed from the uv-data by Tim Shimwell, who provided us with, that provided us compressed frequency cubes of almost 50 GB each. This allowed us to save memory size in our computers; however the compression process, which "only discards the 'noise' from the floating point values without losing any significant information"<sup>1</sup>, becomes particularly significant for us as we decrease the noise when we stack the data and that noise value, which is not important for a single epoch becomes more evident after stacking, and also the values of the polarized intensity change. In practice, the noise and the signals that we measure after having compressed and decompressed the epochs only once, is different from those we measure after having compressed and decompressed even twice. Following this reasoning, the data we have analyzed are different from those produced directly by the processing of uv-data. This problem has been highlighted by our work and will probably be evaluated and solved in the future.

### **Implement the stacking technique**

The analysis of the data was carried out on the supercomputer Vera provided by the Onsala Space Observatory, and we developed a strategy that allowed us the optimization of the processing time and the non-occurrence of RAM memory issues.

We used the programming language Python<sup>2</sup> and related modules developed and optimized for the astrophysics field. Among them, the Astropy<sup>3</sup> package allows the manipulation of fits files. However, a single Stokes frequency cube it cannot even be read as an entire fits file via this package as the size of the data is too large. For this reason, in order to process and analyze our data, we worked with slices of the field for each epoch of size  $12005 \times 151$  pixels

---

<sup>1</sup><https://heasarc.gsfc.nasa.gov/docs/software/fitsio/compression.html>

<sup>2</sup><https://www.python.org/>

<sup>3</sup><https://www.astropy.org/>

(5 deg in right ascension  $\times$  3.75 arcmin in declination, size of 8.7 GB for the Stokes  $Q, U$  frequency cube), which were extracted from the entire field using the `fitscopy`<sup>4</sup> function.

---

<sup>4</sup><https://heasarc.gsfc.nasa.gov/docs/software/fitsio/cexamples.html#fitscopy>

**Table 5.2:** LOFAR ELAIS-N1 datasets used in our work.

ID	LOFAR ID	Date	Duration	$\sigma_{QU}$ ( $\mu\text{Jy beam}^{-1}$ )
009	L229064	2014-05-19	8h00m05s	88
010	L229312	2014-05-20	8h00m05s	88
012	L229673	2014-05-26	8h00m05s	77
013	L230461	2014-06-02	8h00m05s	109
014	L230779	2014-06-03	8h00m05s	73
015	L231211	2014-06-05	8h00m05s	79
016	L231505	2014-06-10	7h20m06s	78
017	L231647	2014-06-12	6h59m58s	84
018	L232981	2014-06-27	4h59m58s	95
019	L233804	2014-07-06	5h00m01s	122
020	L345624	2015-06-07	7h40m06s	82
021	L346136	2015-06-14	7h40m06s	82
022	L346154	2015-06-12	7h40m06s	96
023	L346454	2015-06-17	7h40m06s	96
024	L347030	2015-06-19	7h40m06s	81
026	L347494	2015-06-26	7h40m06s	90
028	L348512	2015-07-01	7h40m06s	104
031	L369530	2015-08-22	7h40m06s	84
032	L369548	2015-08-21	7h40m06s	88

**Table 5.3:** Adapted from Table 1 of Sabater et al. (2021). Columns 1 and 6: internal ID code; Cols 2 and 7: standard LOFAR ID; Cols 3 and 8: date at which the observation started; Cols 4 and 9: total duration of the observation; Cols 5 and 10: noise level in polarization in the  $2.5 \times 2.5$  arcmin<sup>2</sup> central region of the image. The epochs above the solid line belong to Cycle 2, the epochs below to Cycle 4.

## CHAPTER 6

---

### Paper summary

---

In the appended paper we present a polarimetric study at 114.9–177.4 MHz of the European Large Area ISO Survey-North 1 (ELAIS-N1) deep field with LOFAR. The ELAIS-N1 LOFAR deep field is the deepest of the LOFAR Two-Meter Sky Survey (LoTSS) Deep Fields so far, and it has been studied at several radio frequencies. We imaged an area of 25 deg<sup>2</sup> in the Stokes Q and U parameters at 6 arcsec-resolution for 19 eight-hour-long epochs observed in two different LOFAR observing Cycles.

We aligned the polarization angles of the epochs and stacked the datasets, reaching a noise level of 17  $\mu\text{Jy beam}^{-1}$  in the central part of the field. The two observing cycles have a slightly different frequency setup, for this reason the stacking method we developed consists of two steps: first we performed the alignment of the polarization angles in frequency space for the epochs belonging to the same observing cycle, then we combined the two stacked cycles in Faraday space.

We searched for polarized emission in the final stacked data. The search for polarization was performed using two thresholds in the signal-to-noise ratio: an  $8\sigma$  threshold for the blind search in all the field, where we found 25 polarized sources, and a  $6\sigma$  threshold at the location of sources known to be

polarized at 1.4 GHz from Grant et al. (2010), where we found 7 additional polarized sources. We detected 32 sources in total, versus only 6 found in the reference epoch, that corresponds to a number density of 1.28 polarized sources per square degree with median degree of polarization of 1.75%.

We visually inspected in the Stokes  $I$  image Sabater et al. (2021) each detected polarized source to assess its morphology at 150 MHz, and in the 2-4 GHz band by using the Very Large Array Sky Survey (VLASS, Lacy et al. 2020). We also inspected the sources in the optical band in the Sloan Digital Sky Survey (SDSS) to identify the host galaxy, if visible, and find the catalogs the redshift values (Falco et al. 1998; Richards et al. 2009; Ahn et al. 2012; Alam et al. 2015; Albareti et al. 2017; Duncan et al. 2021).

We compared our results with the NVSS RM catalog (Condon et al. 1998), with the LoTSS RM catalog (O’Sullivan et al. 2023) and the work of Herrera Ruiz et al. (2021). We found in general evident signs of beam depolarization at 20 arcsec and excellent agreement in RM measurements.

We also studied the depolarization properties of our 20 polarized sources that have been detected in polarization also at 1.4 GHz by Grant et al. (2010) at 45 arcsec-resolution. The degree of polarization at LOFAR frequencies ( $\Pi_{150\text{MHz}}=1.45\%$ ) is lower than at 1.4 GHz ( $\Pi_{1.4\text{GHz}}=7.98\%$ ), as expected because of the depolarization phenomenon. We observed two sources, with morphology of FR II radio galaxies, that show higher degree of polarization at 150 MHz in the hot-spots, probably due to higher beam depolarization at 1.4 GHz, where the regions of the hot-spots are more diluted.

Furthermore, we modeled the polarized source counts at 150 MHz from the source counts in total flux density for the LOFAR deep field (Mandal et al. 2021) combined with a function of the fractional polarization depending on the statistical properties of our sources. From our study, only the 2% of the sources show polarization at 150 MHz, but the several artifacts in the catalog in total flux density and the cosmic variance in the composition of the counts require further investigation.

## CHAPTER 7

---

### Summary and future work

---

We developed new methods to align the polarization angles and stack the 6 arcsec-resolution Stokes  $Q, U$ -parameter data cubes; the stacked dataset represents the deepest LOFAR polarization data so far, with noise level at the center of the field of  $17 \mu\text{Jy beam}^{-1}$ . In ELAIS-N1 LOFAR deep field ( $25 \text{ deg}^2$ ), after stacking data from 19 epochs, we confidently detected polarization in 32 radio sources (1.28 polarized sources per  $\text{deg}^2$ ), that show a variety of morphologies. Although the number density of polarized sources detected is the highest so far at low frequencies, we still have a low number statistics.

The further optimization of the algorithm for stacking, searching for polarized sources will allow to detect more polarized sources, and the comparison with other frequencies will give the opportunity to study the depolarization properties of sources and to better understand and discern the different contributions to the Faraday rotation along the line of sight.

The developed algorithm can be applied to LoTSS, in the regions of overlapping of pointings, and the other LOFAR deep fields (GOODS-North, Boötes and Lockman Hole), to help us to characterize them and study the cosmic variance.

Furthermore, international baselines are providing a resolution of 0.4 arcsec

in total-intensity data, and the LOFAR community is working to achieve the same resolution in polarization. We expect depolarization to be small at this resolution, but that is as yet unknown territory.

Our work, technically challenging because of the nature of polarization observation, could also be used for future generations of telescopes such as SKA, of which LOFAR represents the largest precursor in terms of effective area and generated data rates.

---

## Bibliography

---

- Ahn, C. P., Alexandroff, R., Allende Prieto, C., et al. 2012, *ApJS*, 203, 21
- Alam, S., Albareti, F. D., Allende Prieto, C., et al. 2015, *ApJS*, 219, 12
- Albareti, F. D., Allende Prieto, C., Almeida, A., et al. 2017, *ApJS*, 233, 25
- Arshakian, T. G. & Beck, R. 2011, *MNRAS*, 418, 2336
- Beck, R. & Gaensler, B. M. 2004, *New A Rev.*, 48, 1289
- Becker, R. H., White, R. L., & Helfand, D. J. 1995, *ApJ*, 450, 559
- Berger, A., Adebahr, B., Herrera Ruiz, N., et al. 2021, *A&A*, 653, A155
- Blandford, R. D. & Rees, M. J. 1974, *MNRAS*, 169, 395
- Brentjens, M. A. & de Bruyn, A. G. 2005, *A&A*, 441, 1217
- Burn, B. J. 1966, *MNRAS*, 133, 67
- Chakraborty, A., Dutta, P., Datta, A., & Roy, N. 2020, *MNRAS*, 494, 3392
- Choudhuri, A. R. 1998, *The physics of fluids and plasmas: an introduction for astrophysicists* (Cambridge University Press)
- Condon, J. J. 1984, *ApJ*, 287, 461
- Condon, J. J. 1988, in *Galactic and Extragalactic Radio Astronomy*, ed. K. I. Kellermann & G. L. Verschuur (Springer-Verlag), 641–678

- Condon, J. J., Cotton, W. D., Greisen, E. W., et al. 1998, *AJ*, 115, 1693
- Condon, J. J. & Ransom, S. M. 2016, *Essential Radio Astronomy* (Princeton University Press)
- de Gasperin, F., Williams, W. L., Best, P., et al. 2021, *A&A*, 648, A104
- Duncan, K. J., Kondapally, R., Brown, M. J. I., et al. 2021, *A&A*, 648, A4
- Duncan, K. J., Sabater, J., Röttgering, H. J. A., et al. 2019, *A&A*, 622, A3
- Falco, E. E., Kochanek, C. S., & Muñoz, J. A. 1998, *ApJ*, 494, 47
- Fanaroff, B. L. & Riley, J. M. 1974, *MNRAS*, 167, 31P
- George, S. J., Stil, J. M., & Keller, B. W. 2012, *PASA*, 29, 214
- Govoni, F., Johnston-Hollitt, M., Agudo, I., et al. 2014, *Cosmic Magnetism Science in the SKA1 Era*, Square Kilometre Array Organisation Science Working Group Assessment Workshop Summary, no. 6, *Cosmic Magnetism*, 26 pages. Published online by the SKA Organisation, March 2014.
- Grant, J. K., Taylor, A. R., Stil, J. M., et al. 2010, *ApJ*, 714, 1689
- Gurnett, D. A. & Bhattacharjee, A. 2005, *Introduction to Plasma Physics* (Cambridge University Press)
- Hales, C. A., Norris, R. P., Gaensler, B. M., et al. 2014, *MNRAS*, 441, 2555
- Hatanaka, T. 1956, *PASJ*, 8, 73
- Heald, G. 2009, in *Cosmic Magnetic Fields: From Planets, to Stars and Galaxies*, ed. K. G. Strassmeier, A. G. Kosovichev, & J. E. Beckman, Vol. 259 (Cambridge University Press), 591–602
- Heald, G., Mao, S., Vacca, V., et al. 2020, *Galaxies*, 8, 53
- Heiles, C. 2002, in *Astronomical Society of the Pacific Conference Series*, Vol. 278, *Single-Dish Radio Astronomy: Techniques and Applications*, ed. S. Stanimirovic, D. Altschuler, P. Goldsmith, & C. Salter, 131–152
- Herrera Ruiz, N., O’Sullivan, S. P., Vacca, V., et al. 2021, *A&A*, 648, A12
- Hutschenreuter, S. & Enßlin, T. A. 2020, *A&A*, 633, A150

- Jelić, V., de Bruyn, A. G., Mevius, M., et al. 2014, *A&A*, 568, A101
- Jelić, V., de Bruyn, A. G., Pandey, V. N., et al. 2015, *A&A*, 583, A137
- Klein, U. & Fletcher, A. 2015, *Galactic and Intergalactic Magnetic Fields* (Springer)
- Kobayashi, H., M. B. L. T. W. 2012, *Probability, Random Processes and Statistical Analysis* (Cambridge University Press)
- Kondapally, R., Best, P. N., Hardcastle, M. J., et al. 2021, *A&A*, 648, A3
- Kronberg, P. P., Kothes, R., Salter, C. J., & Perillat, P. 2007, *ApJ*, 659, 267
- Lacy, M., Baum, S. A., Chandler, C. J., et al. 2020, *PASP*, 132, 035001
- Mahatma, V. H., Hardcastle, M. J., Harwood, J., et al. 2021, *MNRAS*, 502, 273
- Mahatma, V. H., Hardcastle, M. J., Williams, W. L., et al. 2019, *A&A*, 622, A13
- Mandal, S., Prandoni, I., Hardcastle, M. J., et al. 2021, *A&A*, 648, A5
- Mesa, D., Baccigalupi, C., De Zotti, G., et al. 2002, *A&A*, 396, 463
- Mulcahy, D. D., Horneffer, A., Beck, R., et al. 2014, *A&A*, 568, A74
- Murray, W. A. S. & Hargreaves, J. K. 1954, *Nature*, 173, 944
- Neld, A., Horellou, C., Mulcahy, D. D., et al. 2018, *A&A*, 617, A136
- Neronov, A. & Vovk, I. 2010, *Science*, 328, 73
- Ocran, E. F., Taylor, A. R., Vaccari, M., Ishwara-Chandra, C. H., & Prandoni, I. 2020, *MNRAS*, 491, 1127
- Oliver, S., Rowan-Robinson, M., Alexander, D. M., et al. 2000, *MNRAS*, 316, 749
- O'Sullivan, S., Stil, J., Taylor, A. R., et al. 2008, in *The role of VLBI in the Golden Age for Radio Astronomy*, Vol. 9, 107
- O'Sullivan, S. P., Brügggen, M., Vazza, F., et al. 2020, *MNRAS*, 495, 2607

- O’Sullivan, S. P., Machalski, J., Van Eck, C. L., et al. 2019, *A&A*, 622, A16
- O’Sullivan, S. P., Shimwell, T. W., Hardcastle, M. J., et al. 2023, *MNRAS*
- Puglisi, G., Galluzzi, V., Bonavera, L., et al. 2018, *ApJ*, 858, 85
- Rengelink, R. B., Tang, Y., de Bruyn, A. G., et al. 1997, *A&AS*, 124, 259
- Richards, G. T., Myers, A. D., Gray, A. G., et al. 2009, *ApJS*, 180, 67
- Riseley, C. J., Galvin, T. J., Sobey, C., et al. 2020, *PASA*, 37, e029
- Rowan-Robinson, M., Lari, C., Perez-Fournon, I., et al. 2004, *MNRAS*, 351, 1290
- Rudnick, L. & Owen, F. N. 2014, *ApJ*, 785, 45
- Rybicki, G. B. & Lightman, A. P. 1979, *Radiative processes in astrophysics* (Wiley-VCH)
- Ryle, M. & Scheuer, P. A. G. 1955, *Proceedings of the Royal Society of London Series A*, 230, 448
- Sabater, J., Best, P. N., Tasse, C., et al. 2021, *A&A*, 648, A2
- Shimwell, T. W., Hardcastle, M. J., Tasse, C., et al. 2022, *A&A*, 659, A1
- Shimwell, T. W., Röttgering, H. J. A., Best, P. N., et al. 2017, *A&A*, 598, A104
- Shimwell, T. W., Tasse, C., Hardcastle, M. J., et al. 2019, *A&A*, 622, A1
- Sirothia, S. K., Dennefeld, M., Saikia, D. J., et al. 2009, *MNRAS*, 395, 269
- Sokoloff, D. D., Bykov, A. A., Shukurov, A., et al. 1998, *MNRAS*, 299, 189
- Sotomayor-Beltran, C., Sobey, C., Hessels, J. W. T., et al. 2013, *A&A*, 552, A58
- Stil, J. M., Keller, B. W., George, S. J., & Taylor, A. R. 2014, *ApJ*, 787, 99
- Stuardi, C., O’Sullivan, S. P., Bonafede, A., et al. 2020, *A&A*, 638, A48
- Subrahmanyan, R., Ekers, R. D., Saripalli, L., & Sadler, E. M. 2010, *MNRAS*, 402, 2792

- Tasse, C., Shimwell, T., Hardcastle, M. J., et al. 2021, *A&A*, 648, A1
- Taylor, A. R., Stil, J. M., Grant, J. K., et al. 2007, *ApJ*, 666, 201
- Taylor, A. R., Stil, J. M., & Sunstrum, C. 2009, *ApJ*, 702, 1230
- Tucci, M., Martínez-González, E., Toffolatti, L., González-Nuevo, J., & De Zotti, G. 2004, *MNRAS*, 349, 1267
- Tucci, M. & Toffolatti, L. 2012, *Advances in Astronomy*, 2012, 624987
- Vacca, V., Oppermann, N., Enßlin, T., et al. 2016, *A&A*, 591, A13
- Vaccari, M., Lari, C., Angeretti, L., et al. 2005, *MNRAS*, 358, 397
- Van Eck, C. L., Haverkorn, M., Alves, M. I. R., et al. 2018, *A&A*, 613, A58
- White, R. L., Becker, R. H., Helfand, D. J., & Gregg, M. D. 1997, *ApJ*, 475, 479
- Williams, W. L., Hardcastle, M. J., Best, P. N., et al. 2019, *A&A*, 622, A2
- Wilson, T. L., Rohlf, K., & Hüttemeister, S. 2013, *Tools of Radio Astronomy* (Springer)
- Xu, Y., Kronberg, P. P., Habib, S., & Dufton, Q. W. 2006, *ApJ*, 637, 19

